



HAL
open science

Porosity and Compaction State at the Active Pāpaku Thrust Fault in the Frontal Accretionary Wedge of the North Hikurangi Margin

Jade Dutilleul, S. Bourlange, Y. Géraud

► **To cite this version:**

Jade Dutilleul, S. Bourlange, Y. Géraud. Porosity and Compaction State at the Active Pāpaku Thrust Fault in the Frontal Accretionary Wedge of the North Hikurangi Margin. *Geochemistry, Geophysics, Geosystems*, 2021, 22 (10), 10.1029/2020GC009325 . insu-03665926

HAL Id: insu-03665926

<https://insu.hal.science/insu-03665926>

Submitted on 12 May 2022

HAL is a multi-disciplinary open access archive for the deposit and dissemination of scientific research documents, whether they are published or not. The documents may come from teaching and research institutions in France or abroad, or from public or private research centers.

L'archive ouverte pluridisciplinaire **HAL**, est destinée au dépôt et à la diffusion de documents scientifiques de niveau recherche, publiés ou non, émanant des établissements d'enseignement et de recherche français ou étrangers, des laboratoires publics ou privés.



Distributed under a Creative Commons Attribution 4.0 International License



RESEARCH ARTICLE

10.1029/2020GC009325

Key Points:

- Strong contrasts of physical properties including porosity occur across the Pāpaku thrust fault at IODP Site U1518
- The hanging-wall (HW) is overcompacted and shows lower interstitial porosity and higher *P*-wave velocity and resistivity than the footwall
- Porosity suggests differences in maximum burial depth with an uplifted, thrust, and concomitantly eroded HW above the footwall

Supporting Information:

Supporting Information may be found in the online version of this article.

Correspondence to:

J. Dutilleul,
jade.dutilleul@univ-lorraine.fr;
jdutilleul@eri.u-tokyo.ac.jp

Citation:

Dutilleul, J., Bourlange, S., & Géraud, Y. (2021). Porosity and compaction state at the active Pāpaku thrust fault in the frontal accretionary wedge of the north Hikurangi margin. *Geochemistry, Geophysics, Geosystems*, 22, e2020GC009325. <https://doi.org/10.1029/2020GC009325>

Received 27 JUL 2020
 Accepted 18 SEP 2021

© 2021. The Authors.

This is an open access article under the terms of the [Creative Commons Attribution License](https://creativecommons.org/licenses/by/4.0/), which permits use, distribution and reproduction in any medium, provided the original work is properly cited.

Porosity and Compaction State at the Active Pāpaku Thrust Fault in the Frontal Accretionary Wedge of the North Hikurangi Margin

Jade Dutilleul^{1,2} , S. Bourlange¹ , and Y. Géraud¹

¹GeoResources, CNRS, University of Lorraine, Nancy, France, ²Now at Earthquake Research Institute, The University of Tokyo, Tokyo, Japan

Abstract Characterization of the porosity evolution across the sedimentary section entering subduction zones and accreted sediments provide valuable information for understanding the deformation history at accretionary margins and the physico-chemical processes in and around fault zones. International Ocean Discovery Program Expeditions 372 and 375 drilled, logged, and cored the reference section on the incoming plate (Site U1520) and across the active Pāpaku thrust (Site U1518), which is a <30° westward-dipping splay fault in the frontal accretionary wedge at the north Hikurangi margin in a region where tsunami earthquakes and recurrent slow slip events are documented. We observe strong variations of physical properties across the thrust fault. In particular, interstitial porosity increases by ~10% through the fault zone while it exponentially decreases with depth, showing lower values in the hanging-wall (HW; on average, ~36%) than in the footwall (~42%). Based on comparisons of porosity with the compaction curve at Site U1518 with that of reference Site U1520, we infer an overcompaction in the HW and a nearly normal compaction in the footwall of the Pāpaku thrust. We suggest that the porosity pattern across the thrust infers differences in the maximum burial depth of sediments, characterized by an overcompacted HW that has been uplifted, thrust, and concomitantly tectonically eroded above the footwall. Porosity data indicate hydrostatic conditions around the thrust fault contrasting with commonly assumed excess pore pressure at the plate interface.

1. Introduction

Over the last two decades, significant research effort was deployed to better understand how the shallow part of subduction zones accommodates displacement through a wide variety of slip modes, including tsunami earthquakes (e.g., Bilek & Lay, 2002; Seno, 2002) and recently discovered slow earthquakes (e.g., Ito & Obara, 2006; Kodaira et al., 2004; Shelly et al., 2006) and their relation with large damaging earthquakes (Kato et al., 2012; Obara & Kato, 2016; Uchida et al., 2016). In particular, the north Hikurangi margin has attracted the attention of many scientists. Here, the Pacific plate is obliquely subducting beneath the Australian Plate at a velocity of ~4.5–5.5 cm/year (Figure 1a) (Wallace et al., 2004). The shallow plate interface is known to host moderate ($M_w < 7.2$) earthquakes (Wallace et al., 2009; Webb & Anderson, 1998) and large magnitude tsunami earthquakes such as the M_w 6.9–7.1 Poverty Bay and Tolaga Bay earthquakes that occurred in March and May 1947 respectively (Bell et al., 2010, 2014; Doser & Webb, 2003; Hamling et al., 2017) (Figure 1b). Since the installation of a continuously operating global positioning system and dense seismic network in 2002 (Gale et al., 2015), slow slip events have also been detected every 1–2 years along the north Hikurangi margin (Figure 1b) (Bartlow et al., 2014; Beavan et al., 2007; Bell et al., 2010; Douglas et al., 2005; Koulali et al., 2017; McCaffrey et al., 2008; Wallace, 2020; Wallace & Beavan, 2006, 2010; Wallace et al., 2009, 2012, 2016, 2017), some of them being associated with tectonic tremors (Kim et al., 2011; Todd & Schwartz, 2016; Todd et al., 2018). Slow slip events commonly last 1 or 2 weeks and involve 1–3 cm of southeastward surface displacement corresponding to ~7–20 cm of slip on the plate interface (Wallace, 2020; Wallace & Beavan, 2010; Wallace et al., 2004, 2009, 2012, 2016). It has been shown that their source zones coincide with high-amplitude seismic reflectors (Figure 1b), interpreted as fluid-rich subducted sediments (Bassett et al., 2014; Bell et al., 2010; Ellis et al., 2015; Heise et al., 2013; Wallace, 2020). It is commonly accepted that transitional friction stability of which slow slip events are widely interpreted as the expression may result from one or from a combination of the following mechanisms (Saffer & Wallace, 2015): (a) transitional behavior straddling the boundary between unstable friction behavior required

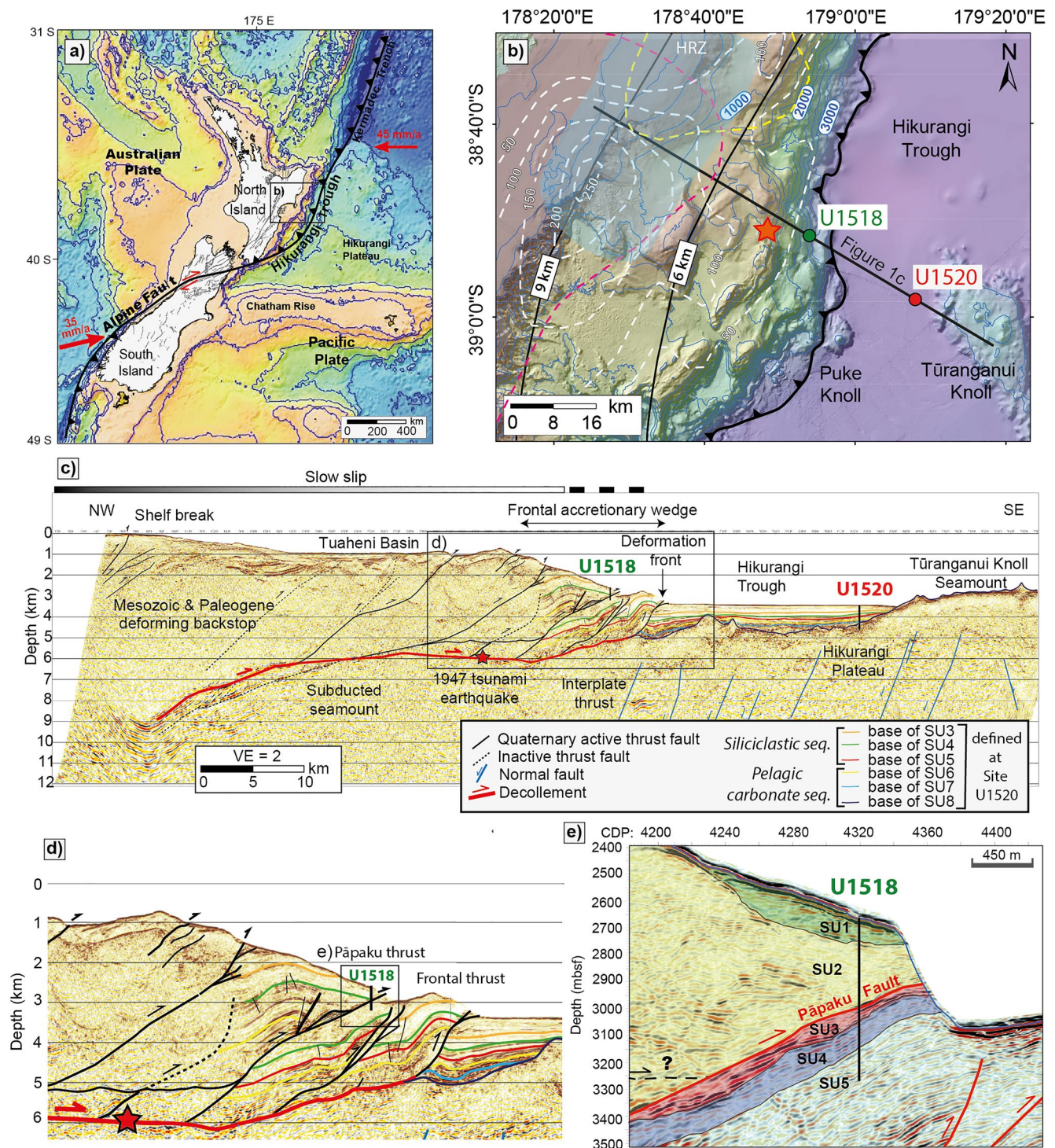


Figure 1.

for stick-slip and stable behavior favoring aseismic creep (Liu & Rice, 2007; McCaffrey et al., 2008), (b) transient elevated pore fluid pressure triggering low effective stress conditions (Audet, 2010; Audet et al., 2009; Han et al., 2017; Ito et al., 2005; Kodaira et al., 2004; Song et al., 2009), and (c) low fault rigidity (Leeman et al., 2016). Transitional friction stability would also contribute to normal earthquake rupture propagation beyond the seismogenic zone and potentially at shallow depths where seafloor deformation is related to tsunamigenesis (Schwartz & Rokosky, 2007). In particular, it has been suggested that rupture propagation

to splay faults may generate tsunamis (Cummins & Kaneda, 2000; Fukao, 1979; Wendt et al., 2009). As observed in subduction zones like Costa Rica (Davis et al., 2015), Ecuador (Vallée et al., 2013), and the Nankai (Kano & Kato, 2020; Uchida et al., 2020; Yamashita et al., 2015; Yokota & Ishikawa, 2020) margins, slow slip events in the north Hikurangi margin occur at exceptionally shallow depths ranging <2–15 km below the seafloor (Saffer et al., 2019a) and may propagate close to the trench as recently captured by a network of absolute pressure gauges deployed offshore (Wallace et al., 2016). However, whether slow slip propagates near the trench along the plate interface and/or splay faults near the deformation front is unresolved (Fagereng et al., 2019; Mouslopoulou et al., 2019; Plaza-Faverola et al., 2016; Shaddock & Schwartz, 2019; Wallace, 2020; Wallace et al., 2016).

To address splay fault activity in the upper plate and relations with seismic and tsunamigenic risks (Pastén-Araya et al., 2021), IODP Expedition 372 logged and IODP Expedition 375 cored Site U1518 in the frontal wedge of the north Hikurangi margin, ~6.5 km west of the deformation front, where distinct imbricate- and splay faults are observed (Fagereng et al., 2019; Saffer et al., 2019b). To study the evolving processes during subduction, Site U1520 was also drilled, cored, and logged on the incoming plate for reference, where a basin is formed by the Hikurangi Trough foredeep overlying the Hikurangi Plateau, ~16 km oceanward of the deformation front (Barnes et al., 2019) (Figures 1b and 1c). Here, the frontal wedge is over-steepened and is inferred to exhibit frontal tectonic erosion related to subducting seamounts (Greve et al., 2020; Pedley et al., 2010; Wallace, 2020). Coring and logging-while-drilling (LWD) at Site U1518 penetrated the hanging-wall (HW) and uppermost footwall, of an active Quaternary thrust fault, named the Pāpaku fault (Saffer et al., 2019b). The Pāpaku fault is a <30° westward-dipping splay fault rooted to the plate interface 10–25 km landward of Site U1518 (Figure 1d). It is inferred to have accommodated ~6 km of shortening within the prism (Fagereng et al., 2019). This thrust is thought to lie within or near the rupture area of the M_w 6.9–7.1 Poverty Bay and Tolaga Bay tsunami earthquakes that occurred in 1947 (Bell et al., 2014; Doser & Webb, 2003; Fagereng et al., 2019) and within or above the slow slip event source area (Barker et al., 2018; Fagereng et al., 2019; Saffer et al., 2019b; Wallace et al., 2016) (Figures 1b and 1c). Core and logging data were used to characterize lithology and sediment composition, deformation structures, physical properties and interstitial fluid geochemistry at Site U1518 during the Expeditions (Saffer et al., 2019b). As part of Expedition 375, three observatories were installed in the HW (~217 mbsf), the fault zone (~323 mbsf), and the footwall (~393 mbsf) of the Pāpaku fault, to monitor the deformation, pore pressure, temperature, and pore fluid geochemistry during the duration of a regional slow slip cycle (Saffer et al., 2019b). These data are expected to be downloaded using a remotely operating vehicle (Saffer et al., 2019b). Although it is currently unclear whether the Pāpaku thrust fault hosts slow slip and/or coseismic slip, the description of varied brittle and ductile deformation structures at Site U1518 indicates that the Pāpaku fault has experienced mixed styles of slip in the past, potentially induced by temporal variations in loading rate and/or pore fluid pressure affecting the frictional properties of the fault (Fagereng et al., 2019).

Here, we address pore pressure distribution and implications for slip style and deformation history at the Pāpaku thrust by documenting fluid content and sediment compaction state at Site U1518 based on geochemical, porosity, and pore structure data. Following previous works (Conin et al., 2011; Dutilleul, Bourlange, Conin, & Géraud, 2020; Dutilleul, Bourlange, Géraud, & Stemmelen, 2020; Henry, 1997; Henry & Bourlange, 2004), we determine the interstitial porosity that is representative of the compaction state of

Figure 1. (a) Tectonic setting of the Hikurangi margin with plate motion indicated by red arrows (modified after Saffer et al., 2019a). (b) Bathymetric map (thin blue lines labeled in meters) of the IODP Expeditions 372/375 study area offshore Gisborne (modified after Saffer et al., 2019a) located on (a) showing the plate boundary (thick black line with teeth), the depth of the subducted plate interface in kilometers below the sea floor (thick black lines, after Williams et al., 2013), the location of IODP Sites U1518 (green dot) and U1520 (red dot), the epicenter location of the 1947 tsunami earthquake (red star), the slip contours of the 2010 Tolaga (yellow) and Gisborne (pink) slow slip events labeled in 40 mm increments, and the October 2014 slow slip event contours (dashed white lines labeled in 50 mm increments) based on Wallace et al. (2016), Wallace (2020), and Barnes et al. (2020). The blue shaded zone represents the high reflectivity zone (HRZ) interpreted as fluid-rich by Bell et al. (2010). The black line represents the location of the seismic cross section shown in (c). (c) Seismic profile 05CM-04 of the accretionary prism and the subducting plate, with collocated IODP drill sites (modified after Saffer et al., 2019a). Interpreted faults and representative seismic stratigraphies with the base of seismic units (SU) defined at Site U1520 (Barnes et al., 2019, 2020) are shown in legend. The red star shows the projected location of March 1947 tsunami earthquake. The panel shows slip distribution of the October 2014 slow slip (after Wallace et al., 2016). VE is vertical exaggeration. (d) Close-up of the frontal accretionary prism from (c). Site U1518 penetrated the Pāpaku thrust, which is one of the splay faults near the deformation front. (e) Close-up of Site U1518 and the Pāpaku thrust from (d) (modified after Saffer et al., 2019b). The main seismic reflectors, seismic stratigraphy and structures are interpreted by Wallace et al. (2019), Barnes et al. (2020), and Fagereng et al. (2019). Note that seismic units were defined independently at Site U1518 (Saffer et al., 2019b) and at Site U1520 (Barnes et al., 2019).

sediments (Brown & Ransom, 1996; Fitts & Brown, 1999; Gamage et al., 2011; Tudge & Tobin, 2013) by correcting the total connected porosity (equivalent to shipboard moisture-and-density (MAD) porosity in Saffer et al., 2019b) from clay-bound water content by conducting geochemical measurements of cation exchange capacity (CEC) and exchangeable cation composition. We further characterize the evolution of pore geometry and size along the depth by conducting mercury injection capillary pressure (MICP) and nuclear magnetic resonance (NMR) measurements that characterize the size of pore throats and bodies, respectively (Bossennec et al., 2018).

We compute the relationship between interstitial porosity and vertical effective stress (that we refer to as compaction curve), and use this curve to compare between Sites U1518 and U1520. Here, we consider the interstitial porosity-vertical effective stress curve at Site U1520 to represent a reference compaction curve of the undeformed sedimentary section prior to subduction. We observe a deviation of interstitial porosity of the deformed sediments at Site U1518 from the reference compaction curve from Site U1520, from which we interpret the hydrologic and tectonic processes that the sediments have likely incurred, by assuming hydrostatic conditions and uniaxial compaction (Conin et al., 2011). The analyses allow us to assess the compaction state of sediments surrounding the Pāpaku thrust fault and evaluate the presence of pore pressure that may affect fault stability and thus fault slip styles along the Pāpaku fault, enabling us to acquire insights on the deformation history at the frontal accretionary wedge and to propose an upper limit for erosion at the Pāpaku thrust.

2. Study Sites, Materials, and Methods

2.1. Geological Setting

2.1.1. Site U1520

At Site U1520, located ~95 km from shore and ~16 km east of the deformation front, the upper oceanic crust, and its sedimentary cover were logged down to ~947 mbsf and cored down to ~1,045 mbsf in ~3,520 m water depth during IODP Expeditions 372 and 375 (see Barnes et al., 2019 for further detail). The sedimentary section is composed of a Quaternary to Paleocene sedimentary cover with Quaternary-aged siliciclastic trench sediments (Units I–III; 0–~510 mbsf) overlying pelagic carbonate formations from Pleistocene to Paleocene (Unit IV; ~510–848 mbsf), above Cretaceous-aged volcanoclastic Units V–VI (~848–1,045 mbsf) of the subducting Hikurangi Plateau as described by Barnes et al. (2019, 2020). The siliciclastic sediments of Units I–III are characterized by gray to greenish silty clay to clayey silt hemipelagites with more or less abundant and thick turbiditic sand and/or silt interbeds, interpreted to be mostly trench-wedge facies (Units I and III) with an undeformed rafted block of the toe domain of the Ruatoria debris flow avalanche (Collot et al., 2001) corresponding to Unit II (~110–222 mbsf) (Barnes et al., 2018). In siliciclastic Units I–III, Dutilleul, Bourlange, Géraud, and Stemmelen (2020) documented relatively low CEC values (in average, 0.14 mol/kg) and bound water content (in average, 5%) typical of clay-rich sediments dominated by illite rather than smectite. Dutilleul, Bourlange, Géraud, and Stemmelen (2020) also showed that these units undergo normal consolidation as interstitial porosity exponentially decreases with depth from ~70% near the seafloor to ~40% at the bottom of Unit III.

2.1.2. Site U1518

In the forelimb of the Pāpaku thrust anticline, ~6.5 km west of the deformation front at ~2,630 m water depth, several boreholes were drilled at Site U1518 to provide logging data, cores and long-term in situ conditions (Saffer et al., 2019b). LWD was carried out at Holes U1518A (0–~118 mbsf) and U1518B (0–~600 mbsf) during IODP Expedition 372 and coring was conducted at Holes U1518E (0–~175 mbsf), and U1518F (~197–495 mbsf) during IODP Expedition 375 less than 50 m south of Holes U1518A and U1518B. From published seismic profiles, the Pāpaku fault corresponds to a negative polarity reflection at the interface between seismic units (SU) 2 and 3 (Saffer et al., 2019b) (Figure 1e), likely related to the variations in petrophysical properties (Cook et al., 2020). At Hole U1518B, the Pāpaku fault zone was localized between ~315 and ~348 mbsf based on major changes in LWD data and from the first occurrence of clustered deformation structures observed in resistivity image logs (Cook et al., 2020; Saffer et al., 2019b). Core recovery was very good in the upper part of the HW (in average, ~92% at Hole U1518E). In the damage zone (DZ) of the HW and the Pāpaku fault zone, core recovery drops to values (~46% at Hole U1518F) commonly

obtained in damaged sections around faults at subduction zones (Fagereng et al., 2019) but the quality of the cores recovered was sufficient to carry out lithological and structural description, as well as physical property measurements (Saffer et al., 2019b). The Pāpaku fault zone was identified between ~304 and ~361 mbsf at Hole U1518F based on a sharp transition from fractured and folded coherent bedding to fault zone rocks with brittle and ductile structures observed in the cores (Fagereng et al., 2019) and an increase in porosity values measured on core samples (Saffer et al., 2019b).

No significant variation in lithology was observed among the HW, the fault zone, and the footwall of the Pāpaku thrust (Figure 2a). The HW corresponds to lithologic Unit I (~0–304 mbsf) consisting of Lower-Mid Pleistocene (>0.53 Ma) hemipelagic silty claystone and fine-grained turbidites sequences. The Pāpaku thrust fault zone is mainly developed in lithologic Unit II (~304–370 mbsf; <0.53 Ma) composed of hemipelagic mudstone alternating with thin and sparse layers of silty mudstone to sandy siltstone. The footwall is mainly composed of relatively undeformed Mid-Upper Pleistocene (<0.53 Ma) bioturbated hemipelagic mudstones of Unit III (~370–492 mbsf) with turbidite sequences. Subunit IIIA is characterized by abundant mass transport deposits (MTDs). It has not been resolved onboard if these MTDs are related to an oversteepened seafloor when frontal accretion initiated at the Pāpaku thrust or to turbidity currents on the trench floor.

Detailed description of the fault zone architecture was published by Fagereng et al. (2019). The HW section is folded with bedding dips ranging 0–50° (Figure 2b), faulted and pervasively fractured from below ~200 mbsf, ~100 m above the Pāpaku fault zone in a zone that we refer to as the HW DZ (Figure 2c). The Pāpaku fault zone is composed of a ~18-m-thick main fault zone (MFZ, Figure 2a) characterized by a mixture of brittle (breccia, faults and fractures) and ductile (flow bands) structures, with ductile features locally overprinted by faults and fractures (Figure 3a). Below, there is a ~21-m-thick zone of gradually decreasing deformation intensity where structures are more ductile than brittle, and a ~10-m-thick subsidiary fault zone (SFZ). The footwall is relatively undeformed although a few ductile-flow deformation structures and occasional faults were identified. Injection structures indicating sediment fluidization were observed in the footwall (Fagereng et al., 2019).

2.2. Sampling and Data

Our study is based on logging data and measurements on 362 core samples acquired at Site U1518 during IODP Expeditions 372–375 and additional post-cruise measurements on 52 samples retrieved from the cruise. Shipboard logging data include *P*-wave velocity, resistivity, neutron porosity, and NMR. Shipboard measurements on core samples include total connected porosity (shipboard MAD analyses) measured on 362 samples, X-ray diffraction (XRD) analyses on 120 samples and interstitial water geochemistry, as well as lithological and structural description (Wallace et al., 2019). We report on newly acquired data measured on 52 core samples from Site U1518 recovered by Expedition 375, which are total connected porosity, CEC, exchangeable cation composition and soluble chloride content (Section 2.3.1.1). These data are used to correct total connected porosity from clay-bound water content (Section 2.3.1.1). We also carried out MICP and NMR experiments on 17 and 14 samples respectively to determine pore size distribution and permeability (Section 2.3.2). The average sampling rate for the study is approximately one sample per core (1 sample each 10 m). We sampled as close as possible (6 cm–4.5 m; in average 0.5 m) to the samples that were squeezed shipboard for interstitial water composition analysis. The samples were stored at chilled temperature (2–8°C) in sealed plastic bags with a sponge saturated with seawater inside the bags to preserve moisture. Shipboard total connected porosity was equal to total connected porosity measured in the laboratory, evidencing that moisture was successfully preserved during transportation of the samples. Porosity data measured on samples were correlated to LWD neutron porosity and NMR porosity data. Data from this study were compared with data from 42 samples from Units I–III at Site U1520 from Dutilleul, Bourlange, Géraud, and Stemmelen (2020).

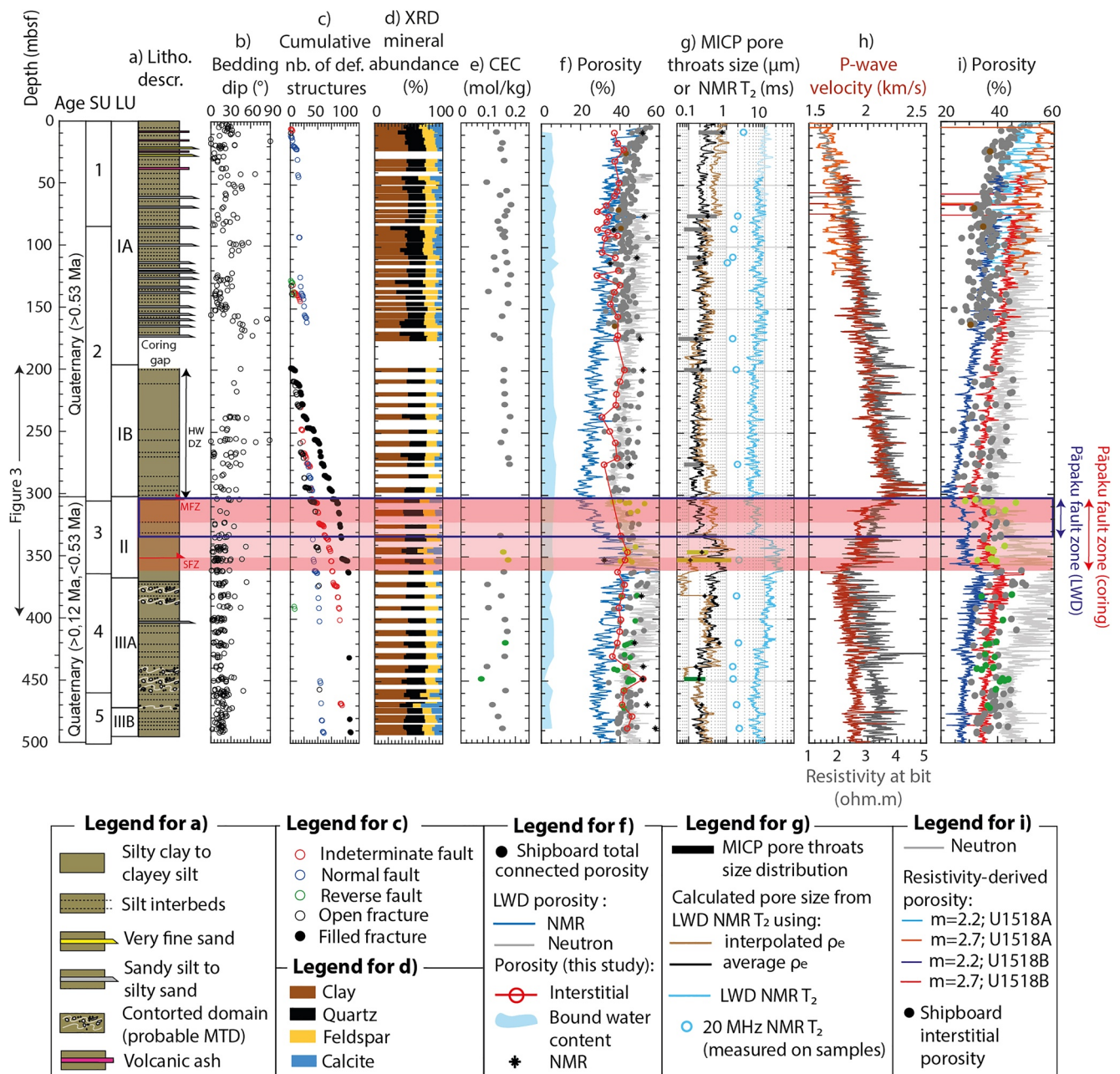


Figure 2. Summary of lithology, mineralogy, structure, and physical properties at Site U1518. (a) Lithostratigraphy showing age, lithological units (LU), seismic units defined at Site U1518 (SU, Figure 1e) and description (see legend) modified after Saffer et al. (2019b). (b) Bedding dip angle measured from the cores and (c) Cumulative number of observed deformation structures (see legend). (d) Mineral assemblage obtained by assemblage from shipboard X-ray diffraction (XRD). (e) Cation exchange capacity. (f) Porosity measured on samples and by logging-while-drilling (LWD) tools (see legend). (g) Pore structure data from MICP and nuclear magnetic resonance (NMR) (see legend). Bars correspond to the range of pore throat diameters where at least 40% of the maximal mercury injection is occurring. The average MICP pore throat diameter is represented by a black dot in the bar. (h) LWD resistivity-at-bit and *P*-wave velocity (see legend). Light orange and light gray correspond to Hole U1518A, dark orange and dark gray correspond to Hole U1518B. (i) Resistivity-derived porosity at Holes U1518A and U1518B using different cementation factors, compared to shipboard interstitial porosity and LWD neutron porosity. The color of the data points and bars in (e, f, g, i) indicates lithology of the samples analyzed: light green for clay (stone), dark green for contorted clay (stone), gray for silty clay (stone), clayey silt (stone), or alternating silt and clay layers and brown for silt (stone) with sand. The red shaded zone corresponds to the location of the Pāpaku fault zone identified from the cores, which are the main fault zone (MFZ) from 304 to 322 mbsf and the subsidiary fault zone (SFZ) from 351 to 361 mbsf. HW DZ indicates the location of the hanging wall damage zone. Note that based on logging data at Hole U1518B, the Pāpaku fault zone is interpreted at depths of ~315–348 mbsf (Cook et al., 2020). LWD data at Hole U1518B were shifted from an average value of ~11 mbsf to fit core data based on the top of the Pāpaku fault zone following Saffer et al. (2019b) and Cook et al. (2020).

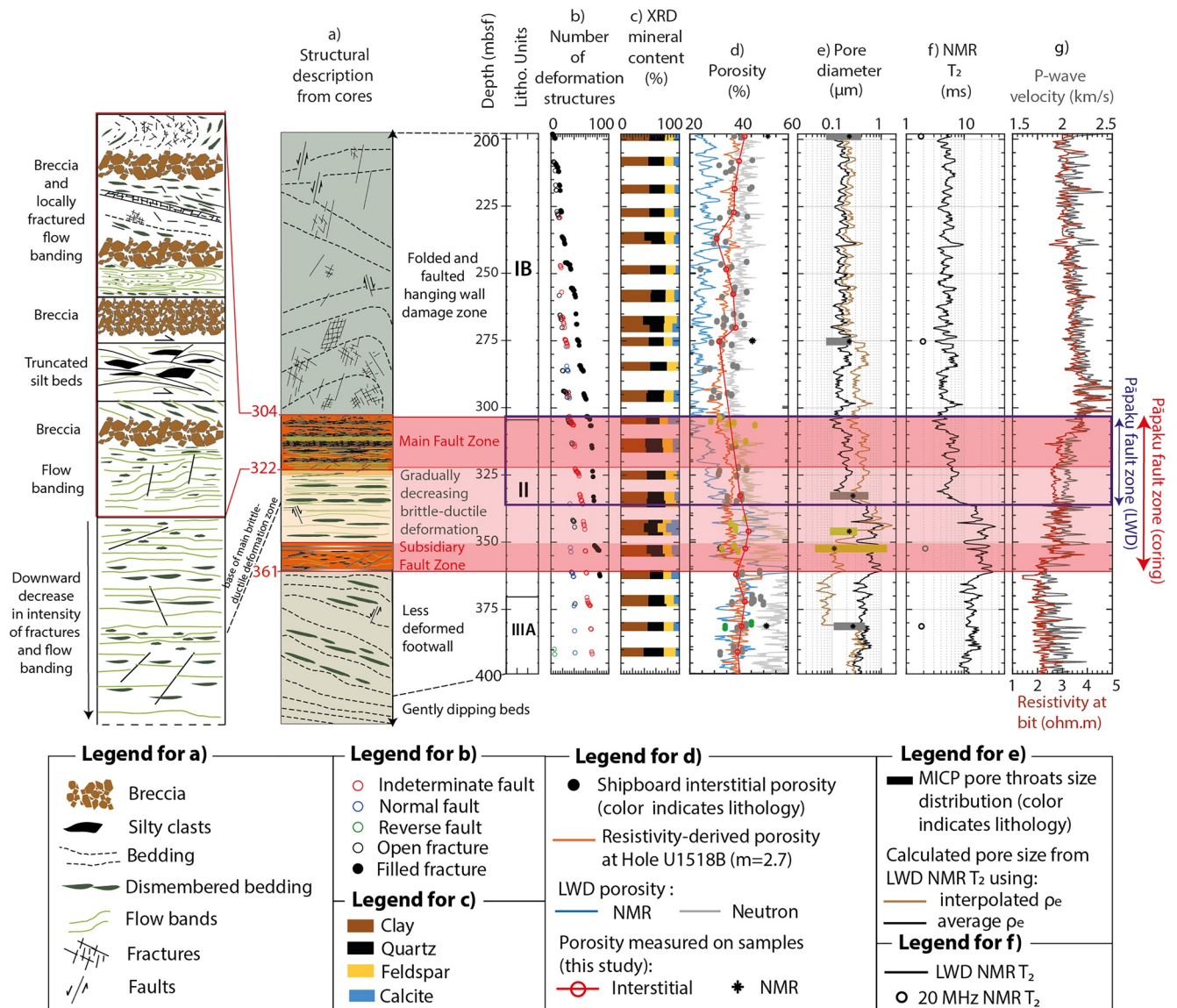


Figure 3. Detailed structural, mineralogical, and physical properties across the Pāpaku Fault zone (304–361 mbsf at coring holes, 315–348 mbsf at logging-while-drilling [LWD] hole) at Site U1518, closed-up from Figure 2. (a) Structural description of ductile and brittle deformation structures (modified after Fagereng et al., 2019; Saffer et al., 2019b) (see legend). (b) Number of brittle deformation structures (see legend). (c) Normalized mineral assemblage obtained from shipboard X-ray diffraction (XRD). (d) Porosity measured on samples and by LWD tools (see legend). (e) Pore structure data from MICP and nuclear magnetic resonance (NMR) (see legend). Bars correspond to the range of pore throat diameters where at least 40% of the maximal mercury injection is occurring. The average MICP pore throat diameter is represented by a black dot. (f) Transverse relaxation time (T_2) from NMR. (g) LWD resistivity-at-bit and P -wave velocity. The color of the data points and bars in (d and e) indicates lithology of the samples analyzed: light green for clay (stone), dark green for contorted clay (stone), gray for silty clay (stone), clayey silt (stone), or alternating silt and clay layers and brown for silt (stone) with sand. LWD data at Hole U1518B were shifted by an average value of ~ 11 mbsf to fit core data based on the top of the Pāpaku fault zone following Saffer et al. (2019b) and Cook et al. (2020).

2.3. Methods

2.3.1. Quantification of Porosity

2.3.1.1. Estimation of Bound Water Content and Interstitial Porosity From CEC, Soluble Chloride Content, and Interstitial Water Composition

Moisture and density analyses were conducted during IODP Expedition 375 which measured the total connected porosity values (Saffer et al., 2019b) that are based on the determination of total water content

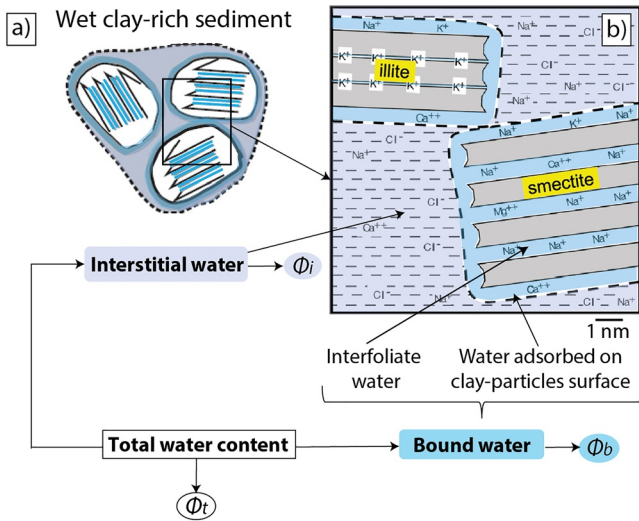


Figure 4. Schematic cartoon (modified after Conin et al., 2011; Salles et al., 2008) showing the relationship between total connected porosity (ϕ_t) representative of total water content, interstitial porosity (ϕ_i) representative of interstitial water and clay bound water (ϕ_b) defined in Equation 3: $\phi_t = \phi_i + \phi_b$. The total water content of a clay-rich sample saturated with seawater includes both interstitial water and clay bound water. The clay bound water (colored in blue) is the water stored in the interlayer space within clay and on clay particle surfaces.

and thus include both interstitial water content and bound water content (Saffer et al., 2019b) (Figure 4). Interstitial water corresponds to the chloride-bearing water located in the pore space that is expellable by compaction-induced dewatering as sediments are buried. Clay bound water includes chloride-free water located in the interlayer space and electrostatically bound on particle surfaces because of the compensation of negatively charged layers by hydrated cations. Clay bound water content is generally poorly affected by compaction (e.g., Bird, 1984; Colten-Bradley, 1987; Dutilleul, Bourlange, Conin, & Géraud, 2020; Fitts & Brown, 1999; Henry & Bourlange, 2004) and transiently released when sediments reach the pressure-temperature (<150°C) window of smectite-to-illite dehydration. Clay bound water can be derived from smectite content quantified from XRD (Brown & Ransom, 1996) or CEC (Conin et al., 2011; Dutilleul, Bourlange, Conin, & Géraud, 2020; Henry, 1997; Henry & Bourlange, 2004). CEC is the number of sites on the mineral surfaces that can exchange ions with interstitial water and is thus a good proxy for bulk hydrous mineral content of the sample. If clay bound water content is known, total connected porosity can be corrected to determine interstitial porosity.

We measured total connected porosity at GeoRessources laboratory, Nancy, France, according to Blum (1997) that was used during IODP Expeditions 372 and 375. This procedure consists of measuring the mass of the sample when it is wet (m_{wet}) and the mass (m_{dry}) and volume (V_{dry} , measured using a Micromeritics® AccuPyc II 1340 helium-displacement pycnometer) after a 24-hr stage of drying in a convection oven at $105^\circ\text{C} \pm 5^\circ\text{C}$ to remove both interstitial and clay bound water. The calculation of total connected porosity ϕ_t and grain density ρ_g is corrected for the precipitation of salt during drying:

$$\phi_t = \frac{V_f}{V_{wet}} = \frac{V_f}{V_f + V_s} \quad (1)$$

and

$$\rho_g = \frac{m_s}{V_s} \quad (2)$$

where $V_f = \frac{m_f}{\rho_f}$ is the volume of pore fluid, $m_f = \frac{m_w}{1-s}$ is the pore fluid mass, $m_w = m_{wet} - m_{dry}$ is the pore water mass, s is the salinity (0.035), ρ_f is the density of pore fluid (1.024 g/cm³), $V_{salt} = \frac{m_{salt}}{\rho_{salt}} = \frac{m_w s}{(1-s)\rho_{salt}}$ is the salt volume, m_{salt} the salt mass, ρ_{salt} the density of salt (2.220 g/cm³), $m_s = m_{wet} - m_f = m_{dry} - m_{salt}$ is the mass of solids excluding salt and $V_s = V_{dry} - V_{salt}$ is the volume of solids excluding salt.

The dry samples were then ground using a Retsch® mixer mill MM200 with agate grinding beads and jars. We conducted three types of geochemical analyses, which are (a) CEC measured by exchange with cobalt-hexamine and ultraviolet-visible spectrometer, (b) exchangeable cation composition (Na^+ , K^+ , Ca^{2+} , Fe^{2+} , and Mg^{2+}) measured by atomic absorption spectrometers Thermo Fisher Scientific® ICE 3300 and Varian® SpectraAA 800 Zeeman, and (c) soluble chloride content per dry mass determined by sequential water extraction (Tessier et al., 1979) and ion chromatography carried out at the Laboratoire Interdisciplinaire des Environnements Continentaux (LIEC) in Nancy and Metz, France. The CEC and soluble chloride content per dry mass are used to determine the clay-bound water content while exchangeable cation composition is used to compute resistivity-derived porosity (Bourlange et al., 2003; Conin et al., 2011; Dutilleul, Bourlange, Conin, & Géraud, 2020; Dutilleul, Bourlange, Géraud, & Stemmelen, 2020; Henry, 1997; Henry & Bourlange, 2004).

Interstitial porosity (ϕ_i) and clay-bound water content (ϕ_b) were determined from the total connected porosity (ϕ_t), the average number n of water molecules per cation charge ($n = 15$ is used corresponding to smectites

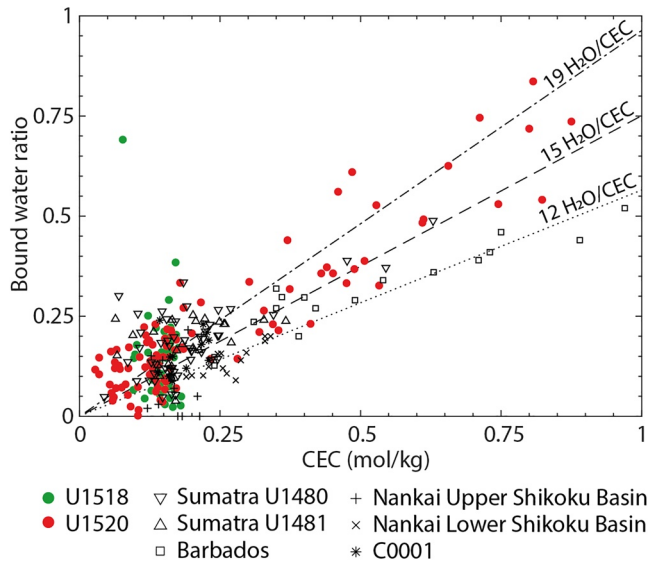


Figure 5. Volume of chloride-free fluid per volume of grain (bound water ratio) versus cation exchange capacity (CEC) at north Hikurangi margin Sites U1518 and U1520 (after Dutilleul, Bourlange, Géraud, & Stemmelen, 2020). Theoretical trends for an ideal two water layers smectite containing 12 or 15 water molecules per cation charge (Henry, 1997) and for a three water layers smectite containing 19 water molecules per cation charge are from Henry and Bourlange (2004) and Conin et al. (2011). Data from the sediment inputs to the north Sumatra subduction zone (IODP Expedition 361) are from Dutilleul, Bourlange, Conin, and Géraud (2020). Data from the sediment inputs to Barbados subduction zone are from Henry (1997). Data from the Nankai Upper and Lower Shikoku Basin are from Henry and Bourlange (2004). Data from Site C0001 (megaspay fault zone of the Nankai accretionary prism) including accretionary wedge and slope apron sediments are from Conin et al. (2011). Data from sediment inputs to the north Sumatra margin (Site U1480) and north Hikurangi margin (Site U1520) plot on the 15 water molecules per cation charge trend (see Dutilleul, Bourlange, Géraud, & Stemmelen, 2020), while sediment inputs to Barbados subduction zone plot on the 12 water molecules per cation charge trend. Other data do not plot on a trend because of too low CEC values (Dutilleul, Bourlange, Conin, & Géraud, 2020; Henry & Bourlange, 2004).

with two layers of water following Dutilleul, Bourlange, Géraud, and Stemmelen (2020) and other studies depicted in Figure 5), the water molar mass M_w ($M_w = 0.018$ kg/mol), the density of pore fluid ρ_f , the grain density ρ_g and the CEC:

$$\phi_i = \phi_t - \phi_b = \phi_t - n \frac{M_w}{\rho_f} \text{CEC} \rho_g (1 - \phi_t) \quad (3)$$

We use the clay bound water content obtained in this study and interpolated for the 362 samples analyzed by moisture and density during Expedition 375 to correct for total connected porosity and determine the shipboard interstitial porosity.

We also use the interstitial porosity to express pore volume loss at specific depth as:

$$\frac{\Delta V}{V_o} = \frac{(\phi_{i0} - \phi_i)}{(1 - \phi_i)} \quad (4)$$

where ΔV is volume loss, V_o is the initial volume, and ϕ_{i0} is the initial interstitial porosity (Saito & Goldberg, 1997).

2.3.1.2. Resistivity-Derived Porosity

Because of (a) a coring gap (~ 175 – 197 mbsf) between lithological Subunit IA and IB, and (b) higher resolution of LWD data than MAD measurements on discrete samples, we use neutron porosity log data and porosity estimated from resistivity-at-bit logs (sampling interval of 15 cm) at Site U1518, in addition to sample measurements. Resistivity-derived porosity was obtained based on the bulk conductivity of the sediments σ , using Revil et al. (1998)'s resistivity model for clay-rich materials with high surface conductivity σ_s . This model is based on Archie's law (Archie, 1942) that links the resistivity-derived porosity ϕ to the formation factor F :

$$F = a \phi^{-m} \quad (5)$$

where m and a are constants. Previous works have shown that resistivity-derived porosity determined using this model with $a = 1$ and a cementation factor $1 \leq m \leq 3.5$ best characterize the interstitial porosity of siliciclastic clay-rich materials (Conin et al., 2011; Dutilleul, Bourlange, Géraud, & Stemmelen, 2020). Because at Site U1518 $\sigma_s / \sigma_{if} \ll 1$, we assume the hypotheses of Bussian (1983) and Bourlange et al. (2003) and express F as:

$$F = \frac{\sigma_{if}}{\sigma} \left[1 + 2 \frac{\sigma_s}{\sigma_{if}} \left(\frac{\sigma_{if}}{\sigma} - 1 \right) \right] \quad (6)$$

The conductivity of the interstitial fluid σ_{if} is determined from the concentration of Cl^- , Na^+ , K^+ , Ca^{2+} , Mg^{2+} , and SO_4^{2-} in pore water (C_{iws}^i) measured during the cruise and seawater (C_{sw}^i), the ionic mobility in the fluid β_f^i and Z_i the number of charges of ions given by Revil et al. (1998), and σ_{sw} the sea water conductivity:

$$\sigma_{if} = \sigma_{sw} \frac{\sum_i (\beta_f^i \times Z_i \times C_{iws}^i)}{\sum_j (\beta_f^j \times Z_j \times C_{sw}^j)} \quad (7)$$

with

$$\sigma_{sw} = 5.32(1 + 0.02(T - 25)) \quad (8)$$

and

$$T(^{\circ}\text{C}) = 1.64 + 35.0 \times 10^{-3} z \quad (9)$$

at Site U1518 (Saffer et al., 2019b).

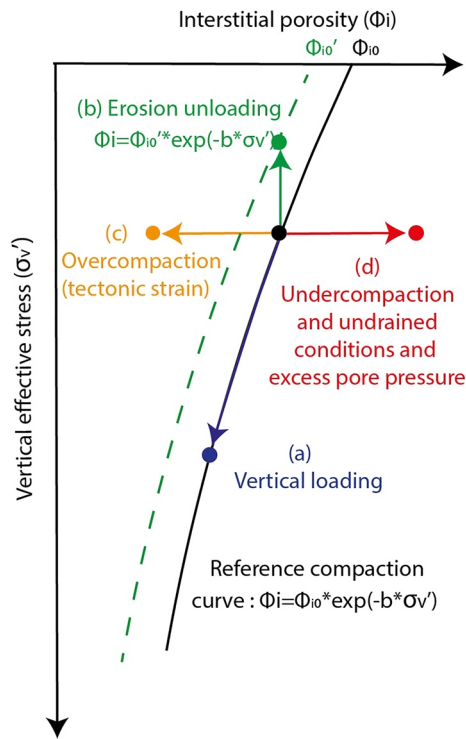


Figure 6. Tectonic (a–c) or hydrologic (d) events resulting in the deviation of interstitial porosity from the reference interstitial porosity–vertical effective stress curve (Equation 12) (modified after Conin et al., 2011).

σ_s is calculated assuming a major contribution of the Stern layer to surface electrical conduction, spherical grains and a linear temperature dependency of the exchangeable cation mobility β_s :

$$\sigma_s = \frac{2}{3} \rho_g \text{CEC} \beta_s \quad (10)$$

2.3.1.3. Determination of Compaction Profiles and Interpretation of Interstitial Porosity Variations in Terms of Tectonic or Hydrologic Events

The progressive burial of poorly consolidated sediments deposited on the oceanic plate as they enter subduction zones undergo mechanical compaction via continuous release of interstitial water and eventually result in lithification (e.g., Bray & Karig, 1985; Fagereng et al., 2018). In drained conditions, compaction-induced dewatering is associated with (a) a reduction and homogenization of pore diameters of which the larger pores collapse first (Daigle, 2014; Dewhurst et al., 1998, 1999), (b) an exponential decrease in porosity (vertical loading in Figure 6a), and (c) possibly a reduction of permeability.

Athy (1930) first expressed normal consolidation considering an exponential decrease of total connected porosity with depth z (Athy, 1930):

$$\phi_t = \phi_0 e^{-bz} \quad (11)$$

where ϕ_0 is the reference porosity at the seafloor and b is the compaction parameter, both varying as a function of lithology, grain size, clay-mineral assemblage, temperature, and sedimentation rate (e.g., Mondol et al., 2007).

Athy's law was then modified accounting that effective porosity (equivalent to interstitial porosity in clay-rich sediments) instead of total connected porosity, exponentially decreases with vertical effective stress σ'_v (MPa) rather than depth (Rubey & Hubbert, 1959; Smith, 1971):

$$\phi_i = \phi_{i0} e^{-b\sigma'_v} \quad (12)$$

Equation 12 is referred to as the compaction curve that is valid if uniaxial vertical stress is assumed. At subduction zones, uniaxial vertical stress is commonly assumed seaward of the trench, where the input section mostly experiences normal consolidation (Figure 6a). Landward, close to the deformation front, sediments may experience non-uniaxial stress such as by lateral tectonic strain (Conin et al., 2011; Henry et al., 2003; Housen et al., 1996; Saffer, 2003; Saffer & Tobin, 2011).

Under uniaxial vertical stress, the total vertical stress σ_v in a sedimentary section is assumed to be equal to the lithostatic pressure P_l (Screaton et al., 2002):

$$\sigma_v = P_l = \sigma'_v + P_f \quad (13)$$

where σ'_v is the vertical effective stress and P_f is the pore fluid pressure.

The vertical effective stress can be calculated from bulk density ρ_B measured on sediment samples as:

$$\sigma'_v(z) = g \int_0^z \rho_B dz - P_f \quad (14)$$

where g is the acceleration due to gravity and P_f is pore fluid pressure in hydrostatic conditions.

The excess pore fluid pressure P_f^* is pore fluid pressure P_f corrected from the hydrostatic pressure P_h :

$$P_f^* = P_f - P_h \quad (15)$$

Based on Equation 15, the excess vertical stress carried by the matrix is:

$$\sigma_v^* = \sigma_v - P_h = \sigma_v' + P_f^* \quad (16)$$

If hydrostatic conditions is assumed (i.e., $P_f^* = 0$, thus $\sigma_v^* = \sigma_v'$), the interstitial porosity data can be used to determine the compaction curve in Equation 12, which serves as a reference curve representing the undeformed sedimentary section prior to subduction.

Assuming similar lithology and initial deposition conditions, deviation of interstitial porosity of sediments of the accretionary wedge from the reference compaction curve can be interpreted in terms of tectonic or hydrologic events that commonly occur in the shallow part of subduction zones, providing insights on spatial variations of tectonic stress, fluid pressure, and stress paths (Bray & Karig, 1985 and references therein; Conin et al., 2011; Saito & Goldberg, 1997). Anomalously low interstitial porosity occurs in overcompacted zones that may have experienced (a) erosional unloading if the compaction profile appears shifted to lower vertical effective stress than the reference compaction curve (Figure 6b) and/or (b) compressive tectonic stress associated with lateral compaction (Figure 6c). Erosional unloading might be associated with a wide range of phenomena such as uplift (e.g., induced by thrusting), oceanic currents or submarine landslides (Conin et al., 2011; Lewis, 1994; Lewis et al., 1998). In contrast, anomalously high interstitial porosity values may reflect undercompacted low-permeability fluid-rich zones where elevated pore pressure results from ineffectual dewatering (Figure 6d). However, it is noted that the combined processes on interstitial porosity variations cannot be deconvoluted based on porosity profiles only (Conin et al., 2011).

Excess pore fluid pressure can be determined based on the amplitude of the positive anomaly of interstitial porosity by introducing P_f^* in Equation 12:

$$\phi_i = \phi_{i0} e^{-b(\sigma_v' - P_f^*)} \quad (17)$$

At Site U1518, we determine compaction curves using shipboard interstitial porosity and resistivity-derived porosity for comparison (Table S1). Although porosity is dependent on numerous parameters like lithology, mineralogy, grain size, and sedimentation rates, we assume that the Quaternary siliciclastic trench sediments forming the HW, the fault zone, and the upper footwall at Site U1518 can be correlated to the undeformed Hikurangi Trough siliciclastic Units I–III at Site U1520 based on the seismic correlation of Barnes et al. (2020) (base of SU4 and SU5 defined at Site U1520, Figures 1c and 1d). Based on this assumption, we compare interstitial porosity data at Site U1518 with the compaction curve determined by Dutilleul, Bourlange, Géraud, and Stemmelen (2020) with interstitial porosity data from Units I–III at Site U1520.

2.3.2. Pore-Network Characterization

MICP and NMR were performed on 17 and 14 samples respectively at the GeoResources laboratory, Nancy, France, to characterize macro- (>50 nm) to mesopore (2–50 nm) size distribution (e.g., Dutilleul, Bourlange, Géraud, & Stemmelen, 2020), according to the International Union of Pure and Applied Chemistry nomenclature (Sing et al., 1985). We also converted higher frequency resolution LWD NMR T_2 in pore size (Section 2.3.2.2).

2.3.2.1. Mercury Injection Capillary Pressure

MICP was performed at room temperature (20°C) using a Micromeritics® AutoPore IV 9500 at GeoResources, Nancy, France, on 17 samples that were previously oven-dried at 105°C ± 5°C for 24 hr. The samples were first degassed under vacuum. Then, mercury is gradually intruded under low-pressure up to a mercury pressure of ~0.2 MPa and the volume of intruded mercury is measured. The volume of intruded mercury is measured stepwise by applying high pressure during an intrusion-extrusion-reintrusion cycle, which provides the size distribution of pore throats (i.e., small pore space at the point where two grain meet, which connects two larger pore volumes) (Bossennec et al., 2018), and mercury trapped porosity (i.e., mercury total connected porosity corrected from mercury-free porosity, as detailed in Rosener & Géraud, 2007). During the first intrusion stage, the mercury fills the connected pore space as mercury injection pressure is progressively increased up to 220 MPa allowing to estimate the distribution of the size of pore throats from 360 μm to 5.7 nm using the Young-Laplace equation:

$$r = \frac{2 \sigma_{\text{Hg}} \cos \theta_{\text{Hg}}}{P_{\text{Hg}}} \quad (18)$$

where r is the pore throat radius (m), σ_{Hg} is the air-mercury interfacial tension (0.485 N/m), θ_{Hg} is the mercury-sediment contact angle (140°), and P_{Hg} is the mercury injection pressure (Pa). This stage also provides mercury total connected porosity (Rosener & Géraud, 2007). During the extrusion stage, the pressure is decreased down to atmospheric pressure with some mercury droplets remaining trapped at narrow pore throats (Li & Wardlaw, 1986a, 1986b) allowing to determine the mercury trapped porosity (Rosener & Géraud, 2007). Mercury trapped porosity reflects the contrast of diameter between pore throats and body size (Bossennec et al., 2018), and is thus a proxy for pore compaction. High mercury trapped porosity suggests narrow throat compared to pore body size thus limited effects of compaction. Reciprocally, low mercury trapped porosity indicates that throats and bodies of pores are of similar sizes due to advanced compaction that tend to squeeze pore bodies.

Finally, mercury-free porosity is reintruded as mercury injection pressure is increased up to the maximum value of 220 MPa.

The distribution of pore throats size derived from MICP was used to determine permeability K_{KT} based on the Katz-Thompson permeability model (Nishiyama & Yokoyama, 2014; Katz & Thompson, 1986, 1987):

$$K_{\text{KT}} = \frac{1}{89} \phi_i \frac{(l_{\text{max}}^h)^3}{l_c} f(l_{\text{max}}^h) \quad (19)$$

where l_c is the pore throat diameter corresponding to the inflexion point of the cumulative MICP curve $f(l)$ of the fractional volume of connected pore throats having diameters of l and larger, and l_{max}^h is the pore throat diameter corresponding to the optimum path for permeability obtained when $l^3 f(l)$ is maximum for $l = l_{\text{max}}^h$ (Katz & Thompson, 1986, 1987).

2.3.2.2. Nuclear Magnetic Resonance

Proton NMR was used to obtain the distribution of the transverse relaxation time T_2 (seconds) which provides information about pore body size distribution (Bossennec et al., 2018) and porosity (Daigle et al., 2014). NMR measurements consist of first applying a static magnetic field B_0 to align seawater hydrogen nuclei at equilibrium. Then, the static pulses B_1 at specific radio frequency is emitted, transiently perturbing the system. This is to measure the time required for hydrogen nuclei to relax to B_0 through diffusion and interaction with the porous media. T_2 is measured in a plane perpendicular to B_0 .

Proton NMR measurements were performed during Expedition 372 with a Schlumberger® proVISION Plus LWD Tool and at the Laboratoire Energies & Mécanique Théorique et Appliquée, Vandoeuvre-lès-Nancy, France, using a Bruker® Minispec Mq20 operating at 20 MHz in this study. For T_2 measurements, we used the Carr-Purcell-Meiboom-Gill (CPMG) pulse sequence (Carr & Purcell, 1954; Meiboom & Gill, 1958) at room temperature (20°C) and atmospheric pressure on 14 saturated core samples with a diameter of 8 mm. In the CPMG sequence, the static pulses B_1 consist of an initial $\pi/2$ pulse orthogonal to B_0 separated by a time τ from a series of π pulses applied with opposite polarity at regular interval 2τ . We used a recycle delay of 0.1 s and a half-echo time τ of 0.04 ms (the minimum time available for this equipment), a gain ranging 70%–80%, 200 echoes per scan and 128 stacked scans. We used UpenWin© software to invert the raw T_2 exponential decay in a smoothed T_2 distribution. We correlated the MICP pore throat radius (μm) to the T_2 measured in the laboratory and to the T_2 measured during Expedition 375 via the NMR logging tool based on the effective relaxivity ρ_e ($\mu\text{m/s}$) using the relation of Marschall et al. (1995):

$$T_2 = \frac{1,000r}{2 \rho_e} \quad (20)$$

Equation 20 (El Sayed, 2016) allowed us to estimate the pore throat radius along the sedimentary section at Site U1518 based on high sampling rate LWD NMR T_2 .

We also determined NMR porosity based on the volume of water V_w in the sample (Daigle et al., 2014):

$$\phi_{\text{NMR}} = \frac{V_w}{V_w + V_s} \quad (21)$$

Here, V_w is determined using a calibration by recording the maximum signal amplitude A_0 (corrected for the gain) during the T_2 measurement for known volume of water: $V_w = 19.762A_0 - 0.092$ ($R^2 = 0.94$). This method was validated using synthetic samples of known porosity.

3. Results

3.1. Clay Mineralogy and CEC

The shipboard total clay content measured by XRD during Expedition 375 is relatively constant (32%–52%, in average ~46%) through Units I–III, with no change from either side of the fault zone (Figure 2d). The CEC values measured in this study are low to intermediate (0.08–0.18 mol/kg, in average 0.15 mol/kg) through the sedimentary section (Figure 2e). Generally, CEC show a positive correlation with total clay content. In Subunit IIIA, the contorted domain where sediments are disturbed by MTDs show lower CEC values (Figures 2a and 2e, ~373–382, ~391, and ~447–458 mbsf). The overall constant range of CEC values at Site U1518 is consistent with the small variation of lithology with depth. These values are in agreement with the post-cruise XRD characterization of the clay mineral assemblage of Underwood et al. (2021) where smectite content in bulk sediment range ~4%–28% (Figure S2). Underwood et al. (2021) also report that illite content in bulk sediments is ~9%–33% and chlorite and kaolinite content is ~3%–12%.

3.2. Porosity

Overall, shipboard total connected porosity averages 43% at Site U1518 but exhibits a large scatter of up to 11% (Figures 2f and 2i). Shipboard total connected porosity exponentially decreases from ~66% near the seafloor to ~40% at the bottom of the HW (Figure 2f) following $\phi_i = 45.89e^{-0.050\sigma'_v}$ ($R^2 = 0.15$) (Table S1). Across the Pāpaku fault zone, total connected porosity gradually increases up to ~54% and exponentially decreases from ~47% down to ~39% in the footwall following $\phi_i = 67.35e^{-0.11\sigma'_v}$ ($R^2 = 0.18$) (Table S1). Similarly, total connected porosity data measured in this study evidence a remarkable contrast between the lower part of the HW (~39%) and the upper footwall (~47%), with the HW exhibiting a general trend of lower values (~42%) compared to the footwall (~47%). In the HW DZ in Subunit IB, total connected porosity values are a few percent higher and decrease more abruptly with increasing depth than Subunit IA. In the footwall, total connected porosity is slightly higher in Subunit IIIB than IIIA.

As a result of relatively constant and low CEC values, bound water content is constant and low (3%–8%, in average 6%) across the section drilled at Site U1518 (Figure 2f).

Because of relatively constant bound water content, the variation pattern of interstitial porosity (Figures 2f and 2i) is very similar to that of total connected porosity. The interstitial porosity measured in this study evidence a contrast by 10% between the bottom of the HW (~32%) and the top of the footwall (~42%) with lower values in the HW (~36% on average) than in the footwall (~42% on average) (Figure 2f). Similarly, shipboard interstitial porosity decreases in the HW from ~60% down to ~34% following an approximate compaction curve of $\phi_i = 39.99e^{-0.06\sigma'_v}$ ($R^2 = 0.14$) (Table S1) with a few percent higher values in the HW DZ (approximately Subunit IB) than in Subunit IA. Shipboard interstitial porosity then gradually increases from ~31% up to ~48% through the Pāpaku fault zone and decreases from ~41% down to ~33% following $\phi_i = 65.45e^{-0.13\sigma'_v}$ ($R^2 = 0.21$) (Table S1) through the footwall (Figure 2i). Compaction curves obtained from resistivity-derived porosity are similar (Table S1). The resulting total pore volume loss obtained from interstitial porosity is twice as high in the HW (~40%) than in the footwall (~20%).

LWD neutron and NMR porosities measured during Expedition 372 (Wallace et al., 2019) show a similar trend as in total connected and interstitial porosities, with significant porosity contrast between the HW and the footwall (Figure 2f). Continuous LWD porosity data are able to record detailed porosity evolution across the Pāpaku fault zone. Both LWD neutron and NMR porosity show a gradual increase across the MFZ, the SFZ and the zone in between. Overall, LWD neutron porosity is consistent with total connected porosity but exhibits larger porosity difference between the HW and the footwall with values higher by a maximum

of 5% compared to those measured on samples in the footwall. In contrast, LWD NMR porosity values are significantly lower than interstitial and total connected porosities, except in Subunit IA where it is generally similar to interstitial porosity. The LWD NMR porosity exhibits the largest porosity shift (~20%) across the Pāpaku fault zone. NMR porosity measured on samples is larger than LWD NMR porosity and is in the range of total connected porosity, except in the Pāpaku fault zone and in Subunit IIIB.

At Hole U1518B, resistivity-derived porosity determined from resistivity-at-bit can be fit with interstitial porosity data using $m = 2.2$ in Subunit IA and $m = 2.7$ from Subunit IB to IIIB (Figure 2i). At Hole U1518A, where resistivity-at-bit shows lower values than recorded at Hole U1518B (Figure 2h), resistivity-derived porosity can be fit with interstitial porosity data using $m = 2$ in the upper part of Subunit IA. At Hole U1518B, the shift toward higher m values occurs across the coring gap (~175–197 mbsf) in the HW that also corresponds to the top of the HW DZ (Figure 2a). Also using the resistivity model developed by Revil et al. (1998), Conin et al. (2011) determined a unique $m = 2.0$ to fit porosity data across the HW, the fault zone and the top of the footwall at Site C0004 in the Nankai accretionary wedge. Based on neutron porosity \varnothing_n and resistivity-at-bit res_{bit} , a single Archie's law $res_{bit} = 68.71\varnothing_n^{-0.85}$ ($R^2 = 0.47$) can be used at Site U1518 (Figure S3). This law approximately corresponds to that of the physical properties of the Pāpaku fault zone and can also be fit to the same curve (Figure S3). In detail, the HW and the footwall plot on slightly different trends, as reported by Saito and Goldberg (1997) at ODP Site 948 located ~5 km landward of the deformation front of the Barbados accretionary complex.

Overall, LWD resistivity and P -wave velocity measured during Expedition 372 are anti-correlated with porosity (Figure 2h). P -wave velocity and resistivity increase from ~1,550 m/s and ~1.8 ohm/m respectively at the seafloor to ~2,200 m/s and ~3.8 ohm/m at the bottom of the HW, and then gradually decrease to ~1,700 m/s and ~1.5 ohm/m in the main Pāpaku fault zone, the SFZ and in between. In the footwall, P -wave velocity and resistivity increase up to ~2,100 m/s and ~2.4 ohm/m.

3.3. Pore Structure

Overall, discrete MICP and NMR measurements (Figure 2g) show that samples are macroporous (i.e., pore diameters >50 nm using the nomenclature of Sing et al., 1985). Samples are characterized by only one family of pore throat size corresponding to 53%–78% (in average, 61%) porosity of the samples. The average diameter of pore throats measured by MICP generally decreases with increasing depth, from ~0.8 μm near the seafloor to ~0.2 μm in Subunit IIIB. The Pāpaku fault zone is an exception with locally larger pore throats. A slight increase in pore size can also be noticed in Subunit IIIB compared to the lower part of Subunit IIIA. These values are in the normal range of pore size of clay-rich siliciclastic marine sediments at this range of depth (e.g., Daigle, 2014; Dugan, 2015). At Site U1518, there is no clear relation between interstitial porosity and mean pore throats diameter, mercury porosity or mercury trapped porosity for the HW, the fault zone, and the footwall based on samples measurements (Figure 7). A weak correlation between porosity and pore throat diameters in clay-rich siliciclastic samples are also reported by Daigle et al. (2014) from the Nankai margin.

Average LWD NMR T_2 and discrete NMR T_2 signals follow the same evolution as pore throats size measured by MICP, although a large discrepancy occurs between the values measured by the LWD tool and on the samples in the laboratory (Figure 2g). T_2 measured in the laboratory is ~2.8 ms near the seafloor and decreases to ~2 ms in the footwall. LWD NMR T_2 steadily decreases from ~9 ms near the seafloor to ~4 ms at the bottom of the HW, increases across the Pāpaku fault zone up to 25 ms, and generally decreases in the footwall to ~7 ms. The discrepancy of values between LWD NMR T_2 and discrete measurements of T_2 on samples could be due to differences of radio-frequency used by the LWD NMR tool and the laboratory measuring device or processing of the data (Barnes et al., 2019; Wallace et al., 2019).

Average relaxivity ρ_e ranges ~13–43 $\mu\text{m/s}$ (in average, 37 $\mu\text{m/s}$) for T_2 measured on samples at 20 MHz and ~1–17 $\mu\text{m/s}$ (in average, 8 $\mu\text{m/s}$) based on LWD T_2 . LWD data provide correlations between neutron porosity and pore throat diameter, showing a similar trend in the HW and the fault zone, but contrasting trend for the footwall (Figure S4).

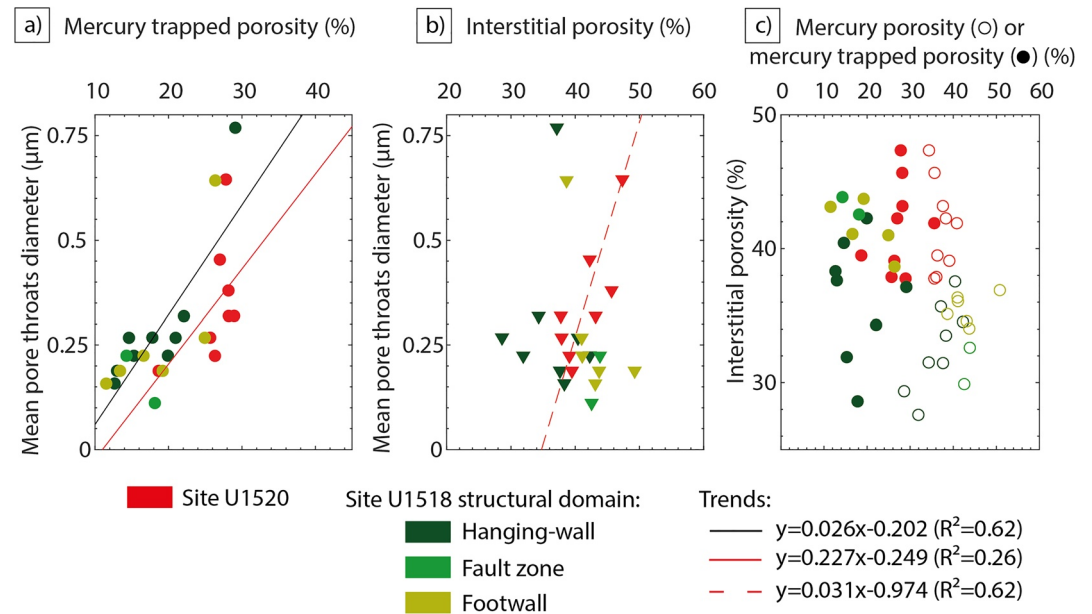


Figure 7. Relations between pore structure and porosity at Site U1518 (green) in the hanging wall, the fault zone, and the upper footwall and in siliciclastic Units I–III from reference Site U1520 (red) (after Dutilleul, Bourlange, Géraud, & Stemmelen, 2020). (a) Relation between mean pore throats diameter and mercury trapped porosity. (b) Relation between mean pore throats diameter and interstitial porosity. (c) Relation among interstitial porosity, mercury porosity (open circles), and mercury trapped porosity (colored circles). Trends were determined using the least square method.

Katz-Thompson permeability determined from MICP decreases with depth from $\sim 7.25 \times 10^{-17} \text{ m}^2$ to $\sim 1.3 \times 10^{-17} \text{ m}^2$ in the HW, 1.2×10^{-17} – $6.3 \times 10^{-18} \text{ m}^2$ in the Pāpaku fault zone and 1.05×10^{-16} – $3.6 \times 10^{-17} \text{ m}^2$ in the footwall (Figure 8).

4. Discussion

In this study, we observe a deviation of interstitial porosity at the Pāpaku thrust at Site U1518 landward of the deformation front from the reference compaction curve from the entering section at reference Site U1520. We interpret the porosity profile at Site U1518 to assess the compaction state of sediments surrounding the Pāpaku thrust fault and get insights on the hydrologic and tectonic processes that the sediments have likely incurred during frontal accretion, by assuming hydrostatic conditions and uniaxial compaction (Conin et al., 2011). The analyses allow us to propose a deformation history at the frontal accretionary wedge with constraints on erosion at the Pāpaku thrust, and to discuss slip style along the Pāpaku fault by evaluating the presence of pore pressure that is commonly considered as the most important factor in creating a weak fault necessary for slow slip events (Audet et al., 2009; Frank et al., 2015; Han et al., 2017).

4.1. Comparison of Interstitial Porosity and Pore Structure Data of Accreted Quaternary Siliciclastic Sequence at Site U1518 With Undeformed Sequence at Site U1520

At Site U1520, interstitial porosity shows exponential decrease with increasing depth from $\sim 66\%$ near the seafloor to $\sim 40\%$ at the bottom of siliciclastic Unit III (Figure 9). When we examine the relationship between porosity and effective vertical stress, the trend at Site U1520 can be fit with an approximate curve of $\phi_i = 46.6e^{-0.029\sigma_v}$ ($R^2 = 0.29$) (Dutilleul, Bourlange, Géraud, & Stemmelen, 2020). We use this curve as the “reference compaction curve,” representative of the undeformed sediments prior to subduction. The compaction profile at Site U1520 indicates normal consolidation (Dutilleul, Bourlange, Géraud, & Stemmelen, 2020), likely resulting from burial compaction-induced dewatering that releases interstitial water prior to subduction (Bray & Karig, 1985).

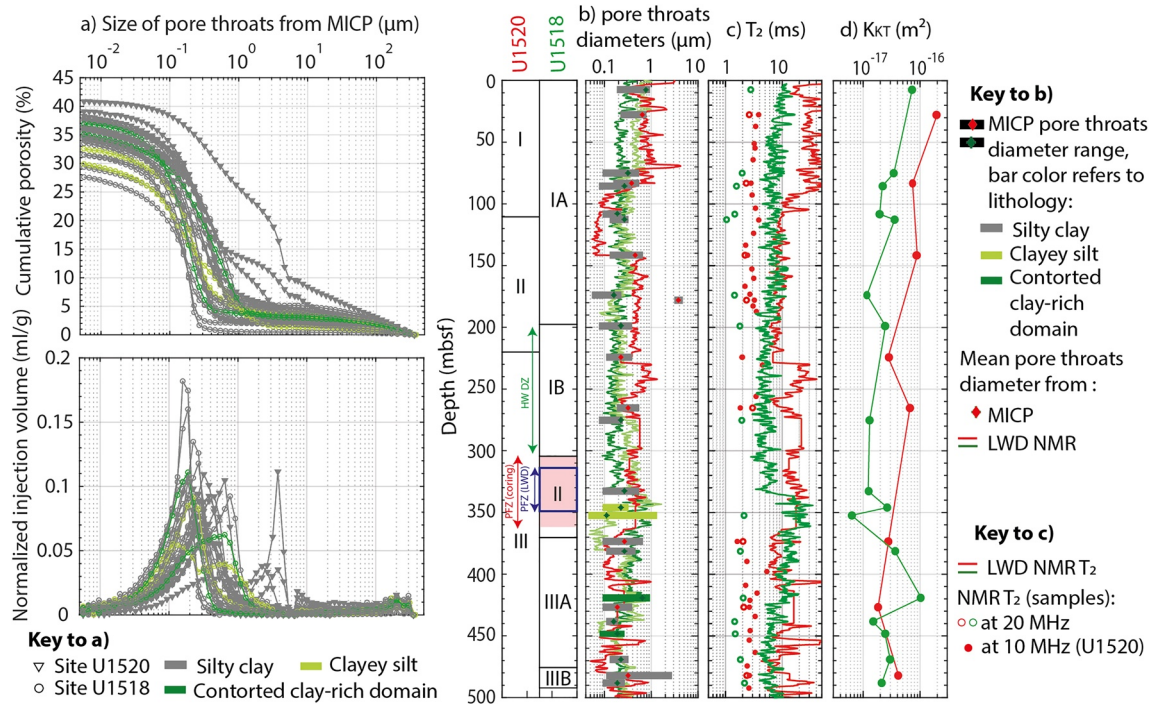


Figure 8. Comparison of (a) mercury injection capillary pressure (MICP) pore throats size distribution, (b) main pore throats diameters, (c) nuclear magnetic resonance (NMR) T_2 , and (d) Katz-Thompson permeability K_{KT} of samples from Site U1518 (green) and Site U1520 (red) siliciclastic Units I–III (Dutilleul, Bourlange, Géraud, & Stemmelen, 2020). The localization of the Pāpaku fault zone at Site U1518 is identified from the cores at ~301–361 mbsf and inferred from logging data at ~315–348 mbsf (marked by blue rectangle). The hanging wall damage zone is distributed within Subunit IB. LWD, logging-while-drilling.

The interstitial porosity values at Site U1518 deviate from the reference compaction curve (Figure 9) and are more scattered than at Site U1520. Standard deviations are 4.3% at Site U1518 and 5.3% in Units I–III at Site U1520. In average, interstitial porosity is ~5–10% lower in the HW at Site U1518 than the reference compaction curve at this range of depths. Across the Pāpaku fault zone and in the upper section of the footwall (~3.3–3.8 MPa in Figure 9), interstitial porosity at Site U1518 increases to similar values at Site U1520 at equivalent depth. Given that the reference compaction curve at Site U1520 represents normal consolidation, the comparison of interstitial porosity data in accreted siliciclastic sequence at Site U1518 with the reference compaction curve at Site U1520 suggests an overcompacted HW, a normally consolidated Pāpaku fault zone and a slightly overcompacted to nearly normally consolidated upper footwall at Site U1518 (Figure 9).

The distinct compaction state between the HW, the fault zone and the top of the footwall inferred in this study from interstitial porosity data is in accordance with the structural observations on cores and interpretations of Saffer et al. (2019b) and Fagereng et al. (2019) and with interpretations of Gray et al. (2019) based on P -wave velocity at the seismic scale. On one hand, the lower porosity overcompacted HW is consistent with the brittle deformation observed on cores (Fagereng et al., 2019; Saffer et al., 2019b). By comparison, the higher porosity and significant lower consolidation of the upper footwall, which correspond to overthrust seafloor material (Morgan et al., 2018) may have, on the opposite, favored the development of ductile deformation structures. The intermediate consolidation state of the fault zone is consistent with a transition from ductile to brittle deformation as the fault grows. On the other hand, Gray et al. (2019) report that the seismic velocity reduction between the HW and the footwall of the Pāpaku thrust (Figure 2h) is small compared to that of other thrusts in the Expeditions 372–375 region, more generally characterized by overcompacted HWs and undercompacted footwalls.

Porosity and pore network characterization from MICP and NMR measurements at Site U1518, show that the trends among interstitial porosity, mean pore throats diameter, mercury porosity, and mercury trapped porosity in undeformed siliciclastic sediments at Site U1520 are similar with those of sediments of the Pāpaku fault zone and the footwall at Site U1518 (Figure 7). However, the HW at Site U1518 is characterized by

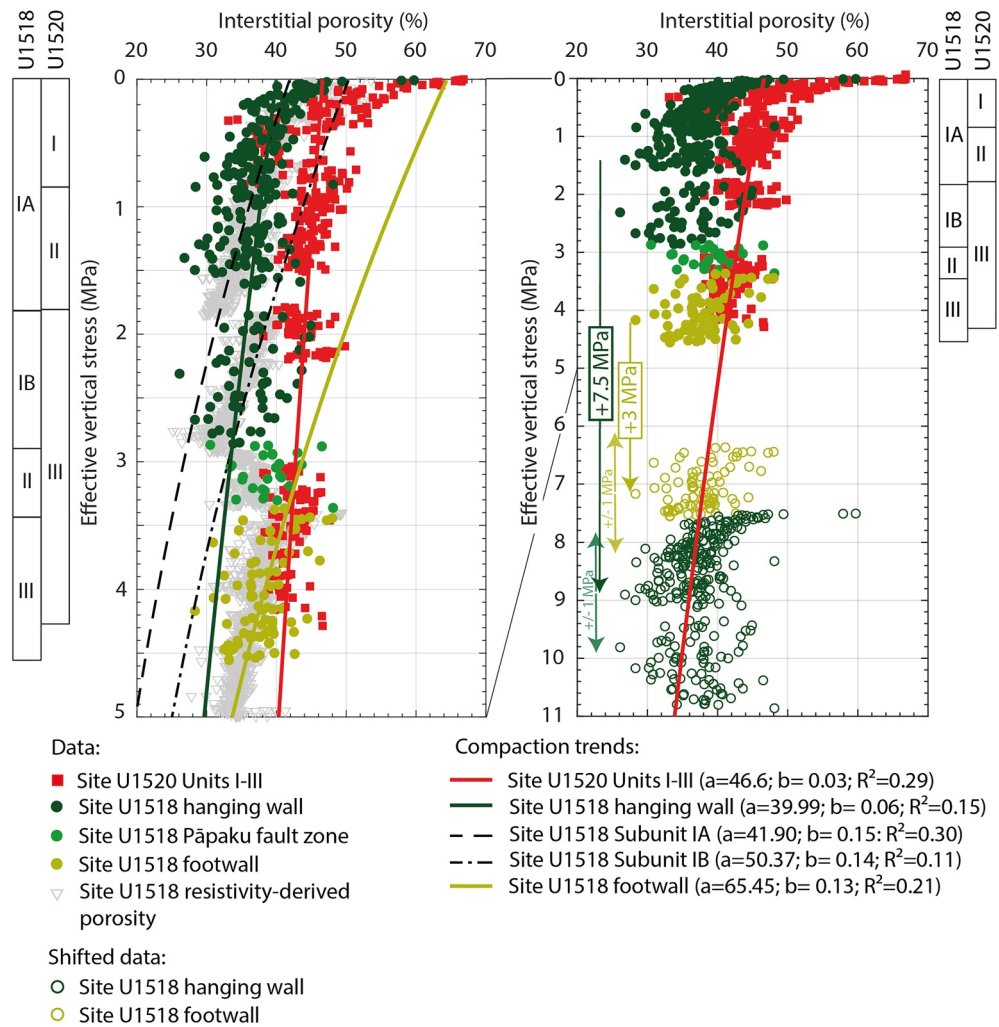


Figure 9. Compaction curves illustrated by the relationship between interstitial porosity and effective vertical stress at Site U1518 (green) and reference Site U1520 siliciclastic Units I-III. Here, sand-rich samples (ranging 0.3–0.9 MPa with interstitial porosity <43%), and very shallow unconsolidated are excluded (Dutilleul, Bourlange, Géraud, & Stemmelen, 2020). The dark green arrow indicates the offset of vertical stress required (+7.5 MPa or ~830 mbsf) for interstitial porosity data of the Pāpaku thrust hanging wall (HW) to match with equivalent porosity on the reference compaction curve of Site U1520. Similarly, the light green arrow indicates the offset of vertical stress required (average offset of +3 MPa or ~330 mbsf) for interstitial porosity data of the footwall to match with the equivalent porosity on the reference compaction curve at Site U1520. The error bars of ~1.0 MPa or ~110 m represent the maximum and minimum shift required for interstitial porosity data of the HW and the footwall at Site U1518 to match with the equivalent porosity on the reference compaction curve at Site U1520.

smaller pores thus lower permeability than expected for present depth at Site U1520, which is consistent with overconsolidation in the HW and normal consolidation in the Pāpaku fault zone and the footwall. Pore diameter measured by MICP (Figure 8a) and estimated from NMR measurements on samples and by LWD NMR (Figure 2g) generally show similar values at Site U1518 and in Site U1520 siliciclastic units, with a general trend of lower values in the HW at Site U1518 than at equivalent depth at Site U1520 (Figure 8b). LWD NMR T_2 and discrete T_2 measurements on samples also show similar range of values at Sites U1518 and U1520, except for two zones in the HW in which T_2 values are lower at Site U1518 than at Site U1520 (Figure 8c). The first zone corresponds to the ~0–90 mbsf interval where the high content of sand-rich turbidite beds at Site U1520 in contrast to the section recorded at Site U1518 may cause the locally high NMR T_2 recorded at Site U1520. The second zone correlates with Subunit IB that also corresponds to the DZ of the overcompacted HW at Site U1518 where both LWD NMR T_2 and discrete T_2 measurements show lower values than at equivalent depth range at Site U1520. The smaller pore size that characterizes the Pāpaku thrust

HW results in a Katz-Thompson permeability ~ 1 order of magnitude lower than measured at equivalent depth at Site U1520 (Figure 8d). In the fault zone and in the footwall, the Katz-Thompson permeability is in the order of permeability estimated at Site U1520, and locally tends to be higher.

4.2. Insights on Compaction State Evolution and Deformation History of Quaternary Siliciclastic Sequence During Accretion

Based on the observed deviations of porosity at Site U1518 from the reference compaction curve of Site U1520 (Figure 9), we propose a simple model where erosion and thrusting are concomitant and potentially associated with excess pore pressure build up and horizontal shortening (Figure 6). These analyses on sediment compaction allows us to interpret the interstitial porosity profile observed at Site U1518 (Figure 9).

Although the HW and the footwall exhibit contrasted interstitial porosity at Site U1518, the footwall follows a normal consolidation trend as typically defined in clay-rich siliciclastic sediments (Kominz et al., 2011; Mondol et al., 2007). Hence, we suggest that both the HW and the footwall sequences have experienced vertical loading as they were progressively buried after deposition on the subducting plate (Figures 6a and 9).

However, the interstitial porosity values of the HW sediments at Site U1518 are significantly lower than the values of the reference Site U1520, implying that the HW has experienced greater burial and vertical effective stress in the past. If we assume that the porosity-vertical effective stress curve at Site U1518 follows the same curve as that of Site U1520, the lower porosities of the HW can be extrapolated to burial depths of $\sim 1,130 \pm 110$ m and vertical effective stress range of $\sim 7.5 \pm 1.0$ MPa (Figure 9). In addition, the slightly lower porosity of the footwall just below the fault zone can be shifted to burial depths of $\sim 330 \pm 110$ m and vertical effective stress range of $\sim 3.0 \pm 1.0$ MPa (Figure 9). Such stress shifts could be the result of uplift due to fault displacement associated with erosion (Figure 6b) and/or lateral tectonic strain (Figure 6c) or a combination of both, although this cannot be constrained based on porosity only. Here, we hypothesize that the stress shifts are better explained by erosion unloading, allowing us to provide an upper limit for erosion in the HW. Erosion is suggested by the truncation of seismic reflectors of the HW on the seismic profile (Figure 1e) and a lower limit of 200–300 m of removed material was defined by French and Morgan (2020).

Based on stress shift values, we infer that the sequence that will later form the HW was buried $\sim 830 \pm 110$ m deeper than present depth at the trench before thrust, thus reaching a maximum thickness of $\sim 1,130 \pm 110$ m. This maximum thickness is in the order of the throw (~ 1.6 – 1.7 km) of the Pāpaku fault zone estimated from seismic line 05CM-04 (Figure 1d). The maximum burial depth of the HW is also in accordance, at the trench, with the depth of the base of the SU4 defined at Site U1520, which is interpreted to represent the same stratigraphy as observed at the base of the HW at Site U1518 (Figure 1d). This suggests that the sediments in the incoming section were overthrust and accreted by the Pāpaku thrust at the deformation front (Morgan et al., 2018), consistent with the current stratigraphic framework. The experienced maximum burial depth of $\sim 1,130 \pm 110$ mbsf in the HW have likely caused greater consolidation of the sediments and developed brittle deformation with pervasive faults and fractures. We explain the stress shift for the footwall by inferring that the footwall was buried at a maximum of $\sim 330 \pm 110$ m deeper than present depth by erosion occurring in at least two stages of uplift by the thrust in an end member scenario (Figure 10). In the first stage, a maximum of ~ 500 m of the HW sequence was initially uplifted and eroded as it was thrust above the footwall. In the second stage, once the HW was thrust over the footwall at a maximum depth of $\sim 630 \pm 110$ m, a maximum of $\sim 330 \pm 110$ m of material were removed resulting in the current thickness of the HW. The inferred contrast in maximal burial depths between the HW and the footwall support the difference in contrasting pore volume loss across the fault estimated in Section 3.2.

Note that each stage actually represents the sum of small-scale erosional events that occurred either during thrusting or once the HW was emplaced above the footwall. Also note that we are assuming a maximum contrast in porosity across the thrust, and therefore the estimated erosion/uplift likely represent maximum values. The actual porosity contrast may be smaller due to an overconsolidation of the HW associated with the thickening of the prism as thrust sheets stack, resulting in compaction and horizontal shortening (Greve et al., 2020; Hamahashi et al., 2013; Saffer & Tobin, 2011; Saito & Goldberg, 1997) (Figure 6c) and/or overpressure in the footwall in the past (Figure 6d), which cannot be quantified based on porosity data only.

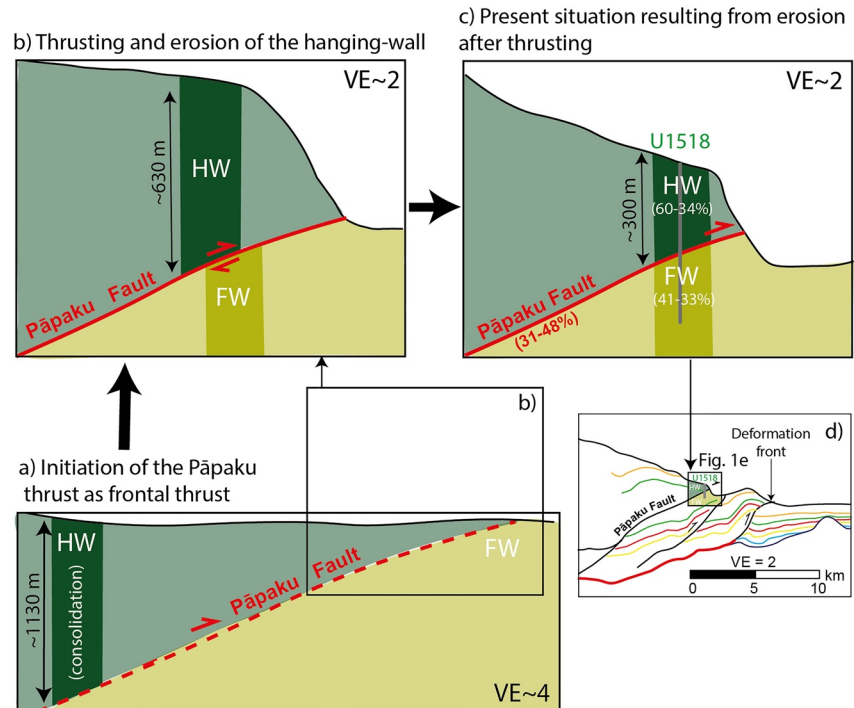


Figure 10. Schematic deformation and erosion history at Site U1518, with (a) normal consolidation of the hanging-wall (HW) and the footwall (FW) before thrusting, (b) thrusting of the HW above the footwall concomitant with a maximum of ~500 m of erosion, and (c) supplementary maximum erosion of ~330 m of the HW once it is set above the footwall to finally reach present setting. Range of shipboard interstitial porosity values for the HW, the fault zone, and the footwall are given in brackets. (d) Present situation at the seaward edge of the north Hikurangi margin (see Figure 1c for legend of colored seismic reflectors) with a zoom in on Site U1518 showing the scale of close-ups (b and c). VE, vertical exaggeration.

Elevated pore fluid pressure developed in the footwall in the past is suggested by the injection features observed in intervals showing ductile flow structures (Section 2.1.2) (Fagereng et al., 2019) indicating dewatering of the footwall (Greve et al., 2020), during burial, exacerbated when the HW was thrust above it (Figure 10b). Because of the lower peak P - T conditions experienced by the footwall compared to the HW and the effect of fluid during faulting (Hamahashi et al., 2013), the footwall was less consolidated and possibly weaker than the HW, leading to the development of ductile deformation structures like flow banding in the footwall (Fagereng et al., 2019). The present nearly normally consolidated interstitial porosity profile in the footwall and the fault zone implies that overpressured fluids were expelled before the second erosion stage, allowing normal consolidation. Fluids may have been transported along the fault zone, as reported by Gray et al. (2019) at the surrounding thrusts characterized by an overcompacted HW and an underconsolidated footwall. Consolidation in the fault zone and the footwall may have favored the formation of brittle deformation structures that overprinted older ductile deformation structures (Section 2.1.2) (Fagereng et al., 2019). Another possibility is that the other thrusts near the deformation front that is thrusting over the footwall of the Pāpaku thrust (Figure 1e) have likely uplifted the sediments in the footwall and caused lower porosity at Site U1518, although this cannot be addressed based on the present data set. Uplift of the footwall may explain why in the lower part of the footwall, porosity tend to plot on a slightly different curve, with lower porosity values than at Site U1520.

Erosion at the Pāpaku thrust is thus limited to between ~200 and 300 m given by French and Morgan (2020) and ~800 m defined in this study. High erosion rate in similar settings have been previously reported at other margins (e.g., Das et al., 2021). Possible erosional mechanisms include gravity-driven flow, oceanic current, and seamount subduction, but are not well constrained at present. Erosion rates close to the upper limit we provide would suggest that, at the time of erosion, the wedge was over-steepened, as still observed

at present (Greve et al., 2020; Pedley et al., 2010; Wallace, 2020) and as suggested by the occurrence of MTDs at the top of the footwall only (Saffer et al., 2019b).

4.3. Insights on Slip Type at the Pāpaku Fault Zone

Interstitial porosity data at Site U1518 in this study does not indicate any fluid-rich zone showing excess pore pressure at present. This result is consistent with Gray et al. (2019) and Cook et al. (2020) who infer no active fluid flow nor elevated pore pressure along the fault zone based on seismic velocities and LWD data. Our data also support the assumption of Cook et al. (2020) that the negative polarity reflection interpreted to correlate with the Pāpaku fault zone results from variations in physical properties rather than elevated fluid content. Together, these observations are not in favor of the possibility for low effective stress and excess pore pressure leading to transitional friction stability as a trigger for slow slip along the Pāpaku fault zone. In that case, slow slip events are rather expected to propagate along the weak plate interface where pore pressure is thought to be elevated (Bassett et al., 2014; Ellis et al., 2015), as suspected at other margins like Cascadia offshore central Oregon (Audet et al., 2009; Han et al., 2017), Nankai (Kamei et al., 2012; Kodaira et al., 2004), Costa Rica (Saffer et al., 2000; Tobin et al., 2001) where slow slip events have been related to fluid-rich plate interface evidenced by low-velocity zones. In contrast, high-velocity drained layers as documented in Cascadia offshore Washington (Han et al., 2017; Peterson & Keranen, 2019) or north Sumatra (Dean et al., 2010; Hüpers et al., 2017) favor large near-trench fast rupture. Alternatively, slow slip behavior could be favored at other seaward thrusts and splay faults that may develop elevated pore pressure (Gray et al., 2019). On the other hand, as suggested by Fagereng et al. (2019), conditional frictional stability prone to slow slip or tsunami earthquake at the Pāpaku thrust could still arise from transient changes of the stress state, for example, induced by transient variations in loading rate and/or fluid pressure. It is possible that the Pāpaku thrust fault ruptured in the past, allowing a discharge of fluid pressure with the drainage of fluids stored in the footwall, as proposed for the plate interface of other margins (Frank et al., 2015; Nakajima & Uchida, 2018; Sibson, 1990; Warren-Smith et al., 2019), before returning, at present, at the beginning of a fluid accumulation stage. This could be verified by retrieving the pore pressure record from the borehole observatories installed at Site U1518 (Saffer et al., 2019b).

5. Conclusion

Based on IODP Expeditions 372 and 375 logging data and sample measurements, we observe strong porosity contrasts between the HW and the footwall of the active Pāpaku splay fault at the north Hikurangi subduction margin drilled at Site U1518. The footwall of the Pāpaku fault is characterized by higher interstitial porosity values (~42% on average) than the fault zone (~41%) and the HW (~36%). By comparing with the porosity profile of the undeformed section of the incoming plate at Site U1520, we infer that the HW of the Pāpaku fault is overconsolidated. Assuming that the deviation of interstitial porosity values results from erosional unloading, we suggest that the HW underwent consolidation as it was buried at greater depth than present prior to subduction, in a setting that is similar to that of the actual trench (~1,100 mbsf), before being thrust above younger and less consolidated sediments of the footwall and unroofed by concomitant erosion. However, other processes may have contributed to shift the sediment porosity from the reference compaction curve, such as (a) the build-up of pore pressure in the footwall in the case of disequilibrium compaction and, (b) poorly drained conditions and folding and thrusting of the HW associated with horizontal shortening. Overall, the Pāpaku thrust at the north Hikurangi margin exhibits lithological, structural, and physical properties similar to that of shallow splay faults in other subduction zones in the early stages of deformation such as the Nankai or Barbados subduction margins. Interstitial porosity data at Site U1518 do not indicate elevated pore pressure at the Pāpaku thrust. The inferred hydrostatic conditions at the Pāpaku thrust suggest that shallow slow slip events that recur in this region of the north Hikurangi margin are more likely to propagate to near the sea floor along the plate interface where elevated pore pressure is inferred, rather than along the splay fault, although slip on the splay fault may be triggered by transient changes of stress state in the case of transient changes of loading rate and fluid pressure.

Data Availability Statement

This research used data provided by the International Ocean Discovery Program (IODP). The shipboard data used are freely available on the LIMS Report Interface Page at web.iodp.tamu.edu/LORE (core photos, analyses of core samples, and interstitial water) or at mlp.ldeo.columbia.edu/logdb/scientific_ocean_drilling (LWD data). Post-cruise data including corrected porosity, CEC, exchangeable cation composition, MICP, and NMR are available in the OTELo Research Data Repository (<https://doi.org/10.24396/ORDAR-31>).

Acknowledgments

The authors greatly acknowledge the funding of the shore-based measurements of CNRS-INSU and IODP-France. The complete crews of IODP Expeditions 372 and 375 are sincerely thanked. The authors thank David Billet, Philippe Rousselle, Maximilien Beuret, Géraldine Kitzinger, and Hervé Marmier from the LIEC laboratory in Nancy and Metz (France) for running CEC, exchangeable cation composition, and soluble chloride content analyses. The manuscript was greatly improved by the comments of anonymous reviewers. The authors also would like to thank Pierre Henry for fruitful discussions associated to the ideas presented in this article.

References

- Archie, G. E. (1942). The electrical resistivity log as an aid in determining some reservoir characteristics. *Transactions of the American Institute of Mining Metallurgical and Petroleum Engineers*, 146, 54–62. <https://doi.org/10.2118/942054-G>
- Athy, L. F. (1930). Density, porosity and compaction of sedimentary rocks. *Bulletin of the American Association of Petroleum Geologists*, 14, 1–24. <https://doi.org/10.1306/3d93289e-16b1-11d7-8645000102c1865d>
- Audet, P. (2010). Temporal variations in crustal scattering structure near Parkfield, California, using receiver functions. *Bulletin of the Seismological Society of America*, 100(3), 1356–1362. <https://doi.org/10.1785/0120090299>
- Audet, P., Bostock, M. G., Christensen, N. I., & Peacock, S. M. (2009). Seismic evidence for overpressured subducted oceanic crust and megathrust fault sealing. *Nature*, 457, 722576–722578. <https://doi.org/10.1038/nature07650>
- Barker, D. H. N., Henrys, S., Caratori Tontini, F., Barnes, P. M., Bassett, D., Todd, E., & Wallace, L. (2018). Geophysical constraints on the relationship between seamount subduction, slow slip, and tremor at the North Hikurangi subduction zone, New Zealand. *Geophysical Research Letters*, 45, 12804–12813. <https://doi.org/10.1029/2018GL080259>
- Barnes, P. M., Ghisetti, F. C., Ellis, S., & Morgan, J. K. (2018). The role of protothrusts in frontal accretion and accommodation of plate convergence, Hikurangi subduction margin, New Zealand. *Geosphere*, 14, 440–468. <https://doi.org/10.1130/GES01552.1>
- Barnes, P. M., Wallace, L. M., Saffer, D. M., Bell, R. E., Underwood, M. B., Fagereng, A., et al. (2020). Slow slip source characterized by lithological and geometric heterogeneity. *Science Advances*, 6, eaay3314. <https://doi.org/10.1126/sciadv.aay3314>
- Barnes, P. M., Wallace, L. M., Saffer, D. M., Pecher, I. A., Petronotis, K. E., LeVay, L. J., et al. (2019). Site U1520. In L. M. Wallace, D. M. Saffer, P. M. Barnes, I. A. Pecher, K. E. Petronotis, & L. J. LeVay (Eds.), *Hikurangi subduction margin coring, logging, and observatories* (Vol. 372B/375). Proceedings of the International Ocean Discovery Program. <https://doi.org/10.14379/iodp.proc.372B375.105.2019>
- Bartlow, N. M., Wallace, L. M., Beavan, R. J., Bannister, S., & Segall, P. (2014). Time-dependent modeling of slow slip events and associated seismicity and tremor at the Hikurangi subduction zone, New Zealand. *Journal of Geophysical Research: Solid Earth*, 119, 734–753. <https://doi.org/10.1002/2013JB010609>
- Bassett, D., Sutherland, R., & Henrys, S. (2014). Slow wavespeeds and fluid overpressure in a region of shallow geodetic locking and slow slip, Hikurangi subduction margin, New Zealand. *Earth and Planetary Science Letters*, 389, 1–13. <https://doi.org/10.1016/j.epsl.2013.12.021>
- Beavan, J., Wallace, L., Douglas, A., & Fletcher, H. (2007). Slow slip events on the Hikurangi subduction interface, New Zealand. In P. Tregoning, & C. Rizos (Eds.), *Dynamic planet, monitoring and understanding a dynamic planet with geodetic and oceanographic tools* (pp. 438–444). Springer. <https://doi.org/10.1007/978-3-540-49350-164>
- Bell, R., Holden, C., Power, W., Wang, X., & Downes, G. (2014). Hikurangi margin tsunami earthquake generated by slow seismic rupture over a subducted seamount. *Earth and Planetary Science Letters*, 397, 1–9. <https://doi.org/10.1016/j.epsl.2014.04.005>
- Bell, R., Sutherland, R., Barker, D. H. N., Henrys, S., Bannister, S., Wallace, L., & Beavan, J. (2010). Seismic reflection character of the Hikurangi subduction interface, New Zealand, in the region of repeated Gisborne slow slip events. *Geophysical Journal International*, 180(1), 34–48. <https://doi.org/10.1111/j.1365-246X.2009.04401.x>
- Bilek, S. L., & Lay, T. (2002). Tsunami earthquakes possibly widespread manifestations of frictional conditional stability: Variability of Greenland accumulation. *Geophysical Research Letters*, 29(14), 18–1–18–4. <https://doi.org/10.1029/2002GL015215>
- Bird, P. (1984). Laramide crustal thickening event in the Rocky Mountain Foreland and Great Plains. *Tectonics*, 3(7), 741–758. <https://doi.org/10.1029/TC003i007p00741>
- Blum, P. (1997). *Physical properties handbook: A guide to the shipboard measurement of physical properties of deep-sea cores* (ODP Tech. Note, 26). Retrieved from <http://www-odp.tamu.edu/publications/tnotes/tn26/INDEX.HTM>
- Bossennec, C., Géraud, Y., Moretti, I., Mattioni, L., & Stemmelen, D. (2018). Pore network properties of sandstones in a fault damage zone. *Journal of Structural Geology*, 110, 24–44. <https://doi.org/10.1016/j.jsg.2018.02.003>
- Bourlange, S., Henry, P., Moore, J. C., Mikada, H., & Klaus, A. (2003). Fracture porosity in the décollement zone of Nankai accretionary wedge using Logging while Drilling resistivity data. *Earth and Planetary Science Letters*, 209, 103–112. [https://doi.org/10.1016/S0012-821X\(03\)00082-7](https://doi.org/10.1016/S0012-821X(03)00082-7)
- Bray, C. J., & Karig, D. E. (1985). Porosity of sediments in accretionary prisms and some implications for dewatering processes. *Journal of Geophysical Research*, 90, 768–778. <https://doi.org/10.1029/JB090iB01p00768>
- Brown, K. M., & Ransom, B. (1996). Porosity corrections for smectite-rich sediments: Impact on studies of compaction, fluid generation, and tectonic history. *Geology*, 24, 843–846. [https://doi.org/10.1130/0091-7613\(1996\)024<0843:pcfhrs>2.3.co;2](https://doi.org/10.1130/0091-7613(1996)024<0843:pcfhrs>2.3.co;2)
- Bussian, A. E. (1983). Electrical conductance in a porous medium. *Geophysics*, 48(9), 1258–1268. <https://doi.org/10.1190/1.1441549>
- Carr, H. Y., & Purcell, E. M. (1954). Effects of diffusion on free precession in nuclear magnetic resonance experiments. *Physical Review*, 94(3), 630–638. <https://doi.org/10.1103/PhysRev.94.630>
- Collot, J.-Y., Lewis, K., Lamarche, G., & Lallemand, S. (2001). The giant Ruatoria debris avalanche on the northern Hikurangi margin, New Zealand: Result of oblique seamount subduction. *Journal of Geophysical Research*, 106, 19271–19297. <https://doi.org/10.1029/2001JB900004>
- Colten-Bradley, V. A. (1987). Role of pressure in smectite dehydration—Effects on geopressure and smectite-to-illite transformation. *Bulletin of the American Association of Petroleum Geologists*, 71(11), 1414–1427. <https://doi.org/10.1306/703C8092-1707-11D7-8645000102C1865D>
- Conin, M., Henry, P., Bourlange, S., Raimbourg, H., & Reuschlé, T. (2011). Interpretation of porosity and LWD resistivity from the Nankai accretionary wedge in light of clay physicochemical properties: Evidence for erosion and local overpressuring. Porosity and LWD resistivity from Nankai. *Geochemistry, Geophysics, Geosystems*, 12. <https://doi.org/10.1029/2010GC003381>

- Cook, A. E., Paganoni, M., Clennell, M. B., McNamara, D. D., Nole, M., Wang, X., et al. (2020). Physical properties and gas hydrate at a near-seafloor thrust fault, Hikurangi margin, New Zealand. *Geophysical Research Letters*, *47*. <https://doi.org/10.1029/2020GL088474>
- Cummins, P. R., & Kaneda, Y. (2000). Possible splay fault slip during the 1946 Nankai earthquake. *Geophysical Research Letters*, *27*, 2725–2728. <https://doi.org/10.1029/1999GL011139>
- Daigle, H. (2014). Microporosity development in shallow marine sediments from the Nankai Trough. *Marine Geology*, *357*, 293–303. <https://doi.org/10.1016/j.margeo.2014.09.041>
- Daigle, H., Thomas, B., Rowe, H., & Nieto, M. (2014). Nuclear magnetic resonance characterization of shallow marine sediments from the Nankai Trough, Integrated Ocean Drilling Program Expedition 333: NMR of Nankai Trough sediments. *Journal of Geophysical Research: Solid Earth*, *119*, 2631–2650. <https://doi.org/10.1002/2013JB010784>
- Das, P., Lin, A. T.-S., Chen, M.-P. P., Miramontes, E., Liu, C.-S., Huang, N.-W., et al. (2021). Deep-sea submarine erosion by the Kuroshio Current in the Manila accretionary prism, offshore Southern Taiwan. *Tectonophysics*, *807*, 228813. <https://doi.org/10.1016/j.tecto.2021.228813>
- Davis, E. E., Villinger, H., & Sun, T. (2015). Slow and delayed deformation and uplift of the outermost subduction prism following ETS and seismogenic slip events beneath Nicoya Peninsula, Costa Rica. *Earth and Planetary Science Letters*, *410*, 117–127. <https://doi.org/10.1016/j.epsl.2014.11.015>
- Dean, S. M., McNeill, L. C., Henstock, T. J., Bull, J. M., Gulick, S. P. S., Austin, J. A., et al. (2010). Contrasting décollement and prism properties over the Sumatra 2004–2005 earthquake rupture boundary. *Science*, *329*, 207–210. <https://doi.org/10.1126/science.1189373>
- Dewhurst, D. N., Aplin, A. C., & Sarda, J. P. (1999). Influence of clay fraction on pore-scale properties and hydraulic conductivity of experimentally compacted mudstones. *Journal of Geophysical Research*, *104*(B12), 29261–29274. <https://doi.org/10.1029/1999jb900276>
- Dewhurst, D. N., Aplin, A. C., Sarda, J. P., & Yang, Y. (1998). Compaction-driven evolution of porosity and permeability in natural mudstones: An experimental study. *Journal of Geophysical Research*, *103*, 651–661. <https://doi.org/10.1029/97jb02540>
- Doser, D. I., & Webb, T. H. (2003). Source parameters of large historical (1917–1961) earthquakes, North Island, New Zealand. *Geophysical Journal International*, *152*, 795–832. <https://doi.org/10.1046/j.1365-246X.2003.01895.x>
- Douglas, A., Beavan, J., Wallace, L., & Townend, J. (2005). Slow slip on the northern Hikurangi subduction interface, New Zealand. *Geophysical Research Letters*, *32*, 16. <https://doi.org/10.1029/2005GL023607>
- Dugan, B., & the Expedition 338 Scientists. (2015). Data report: Porosity and pore size characteristics of sediments from Site C0002 of the Nankai Trough determined by mercury injection. In M. Strasser, B. Dugan, K. Kanagawa, G. F. Moore, S. Toczko, & L. Maeda (Eds.), *Proceedings of IODP (Vol. 338)*. Integrated Ocean Drilling Program. <https://doi.org/10.2204/iodp.proc.338.202.2015>
- Dutilleul, J., Bourlange, S., Conin, M., & Géraud, Y. (2020). Quantification of bound water content, interstitial porosity and fracture porosity in the sediments entering the North Sumatra subduction zone from cation exchange capacity and IODP Expedition 362 resistivity data. *Marine and Petroleum Geology*, *111*, 156–165. <https://doi.org/10.1016/j.marpetgeo.2019.08.007>
- Dutilleul, J., Bourlange, S., Géraud, Y., & Stemmelen, D. (2020). Porosity, pore structure, and fluid distribution in the sediments entering the northern Hikurangi margin, New Zealand. *Journal of Geophysical Research: Solid Earth*, *125*, e2020JB020330. <https://doi.org/10.1029/2020JB020330>
- Ellis, S., Fagereng, Å., Barker, D., Henrys, S., Saffer, D., Wallace, L., et al. (2015). Fluid budgets along the northern Hikurangi subduction margin, New Zealand: The effect of a subducting seamount on fluid pressure. *Geophysical Journal International*, *202*, 277–297. <https://doi.org/10.1093/gji/ggv127>
- El Sayed, A. M. (2016). Petrophysical properties of clastic reservoirs using NMR relaxometry and mercury injection data: Bahariya formation, Egypt. *IOP Conference Series: Earth and Environmental Science*, *44*, 042018. <https://doi.org/10.1088/1755-1315/44/4/042018>
- Fagereng, Å., Diener, J. F. A., Ellis, S., & Remitti, F. (2018). Fluid-related deformation processes at the up- and down-dip limits of the subduction thrust seismogenic zone: What do the rocks tell us? In T. Byrne, M. B. Underwood, D. Fisher, L. McNeill, D. Saffer, K. Ujiie, & A. Yamaguchi (Eds.), *Geology and tectonics of subduction zones: A tribute to Gaku Kimura* (Geological Society of America Special Paper 534, pp. 187–215). [https://doi.org/10.1130/2018.2534\(12\)](https://doi.org/10.1130/2018.2534(12))
- Fagereng, Å., Savage, H. M., Morgan, J. K., Wang, M., Meneghini, F., Barnes, P. M., et al. (2019). Mixed deformation styles observed on a shallow subduction thrust, Hikurangi margin, New Zealand. *Geology*, *47*, 6–876. <https://doi.org/10.1130/G46367.1>
- Fitts, T. G., & Brown, K. M. (1999). Stress-induced smectite dehydration: Ramifications for patterns of freshening and fluid expulsion in the N. Barbados accretionary wedge. *Earth and Planetary Science Letters*, *172*, 179–197. [https://doi.org/10.1016/S0012-821X\(99\)00168-5](https://doi.org/10.1016/S0012-821X(99)00168-5)
- Frank, W. B., Shapiro, N. M., Husker, A. L., Kostoglodov, V., Bhat, H. S., & Campillo, M. (2015). Along-fault pore-pressure evolution during a slow-slip event in Guerrero, Mexico. *Earth and Planetary Science Letters*, *413*, 135–143. <https://doi.org/10.1016/j.epsl.2014.12.051>
- French, M. E., & Morgan, J. K. (2020). Pore fluid pressures and strength contrasts maintain frontal fault activity, northern Hikurangi margin, New Zealand. *Geophysical Research Letters*, *47*. <https://doi.org/10.1029/2020gl089209>
- Fukao, Y. (1979). Tsunami earthquakes and subduction processes near deep-sea trenches. *Journal of Geophysical Research*, *84*, 2303. <https://doi.org/10.1029/JB084iB05p02303>
- Gale, N., Gledhill, K., Chadwick, M., & Wallace, L. (2015). The Hikurangi margin continuous GNSS and seismograph network of New Zealand. *Seismological Research Letters*, *86*, 101–108. <https://doi.org/10.1785/0220130181>
- Gamage, K., Scream, E., Bekins, B., & Aiello, I. (2011). Permeability-porosity relationships of subduction zone sediments. *Marine Geology*, *279*, 19–36. <https://doi.org/10.1016/j.margeo.2010.10.010>
- Gray, M., Bell, R. E., Morgan, J. V., Henrys, S., & Barker, D. H. N., & the IODP Expedition 372 and 375 science parties. (2019). Imaging the shallow subsurface structure of the north Hikurangi subduction zone, New Zealand, using 2-D full-waveform inversion. *Journal of Geophysical Research: Solid Earth*, *124*, 9049–9074. <https://doi.org/10.1029/2019JB017793>
- Greve, A., Kars, M., Zerbst, L., Stipp, M., & Hashimoto, Y. (2020). Strain partitioning across a subduction thrust fault near the deformation front of the Hikurangi subduction margin, New Zealand: A magnetic fabric study on IODP Expedition 375 Site U1518. *Earth and Planetary Science Letters*, *542*, 116322. <https://doi.org/10.1016/j.epsl.2020.116322>
- Hamahashi, M., Saito, S., Kimura, G., Yamaguchi, A., Fukuchi, R., Kameda, J., et al. (2013). Contrasts in physical properties between the hanging wall and footwall of an exhumed seismogenic megasplay fault in a subduction zone—An example from the Nobeoka Thrust Drilling Project: Physical property of exhumed splay fault. *Geochemistry, Geophysics, Geosystems*, *14*, 5354–5370. <https://doi.org/10.1002/2013GC004818>
- Hamling, I. J., Hreinsdóttir, S., Clark, K., Elliott, J., Liang, C., Fielding, E., et al. (2017). Complex multifault rupture during the 2016 Mw 7.8 Kaikōura earthquake, New Zealand. *Science*, *356*, eaam7194. <https://doi.org/10.1126/science.aam7194>
- Han, S., Bangs, N. L., Carbotte, S. M., Saffer, D. M., & Gibson, J. C. (2017). Links between sediment consolidation and Cascadia megathrust slip behaviour. *Nature Geoscience*, *10*, 954–959. <https://doi.org/10.1038/s41561-017-0007-2>

- Heise, W., Caldwell, T. G., Bertrand, E. A., Hill, G. J., Bennie, S. L., & Ogawa, Y. (2013). Changes in electrical resistivity track changes in tectonic plate coupling. *Geophysical Research Letters*, *40*, 5029–5033. <https://doi.org/10.1002/grl.50959>
- Henry, P. (1997). Relationship between porosity, electrical conductivity and cation exchange capacity in Barbados wedge sediments. *Proceedings of the Ocean Drilling Program, Scientific Results*, *156*, 137–149. <https://doi.org/10.2973/odp.proc.sr.156.020.1997>
- Henry, P., & Bourlange, S. (2004). Smectite and fluid budget at Nankai IODP sites derived from cation exchange capacity. *Earth and Planetary Science Letters*, *219*, 129–145. [https://doi.org/10.1016/s0012-821x\(03\)00694-0](https://doi.org/10.1016/s0012-821x(03)00694-0)
- Henry, P., Jouniaux, L., Screaton, E. J., Hunze, S., & Saffer, D. M. (2003). Anisotropy of electrical conductivity record of initial strain at the toe of the Nankai accretionary wedge. *Journal of Geophysical Research*, *108*. <https://doi.org/10.1029/2002JB002287>
- Housen, B., Tobin, H., Labaume, P., Leitch, E., Maltman, A., & Ocean Drilling Program Leg 156 Shipboard Science Party. (1996). Strain decoupling across the decollement of the Barbados accretionary prism. *Geology*, *24*(2), 127–130. [https://doi.org/10.1130/0091-7613\(1996\)024<0127:sdato>2.3.co;2](https://doi.org/10.1130/0091-7613(1996)024<0127:sdato>2.3.co;2)
- Hüpers, A., Torres, M. E., Owari, S., McNeill, L. C., Dugan, B., Henstock, T. J., et al. (2017). Release of mineral-bound water prior to subduction tied to shallow seismogenic slip off Sumatra. *Science*, *356*, 841–844. <https://doi.org/10.1126/science.aal3429>
- Ito, A., Fujie, G., Miura, S., Kodaira, S., Kaneda, Y., & Hino, R. (2005). Bending of the subducting oceanic plate and its implication for rupture propagation of large interplate earthquakes off Miyagi, Japan, in the Japan Trench subduction zone. *Geophysical Research Letters*, *32*, L05310. <https://doi.org/10.1029/2004gl022307>
- Ito, Y., & Obara, K. (2006). Very low frequency earthquakes within accretionary prisms are very low stress-drop earthquakes. *Geophysical Research Letters*, *33*, L09302. <https://doi.org/10.1029/2006GL025883>
- Kamei, R., Pratt, R. G., & Tsuji, T. (2012). Waveform tomography imaging of a megasplay fault system in the seismogenic Nankai subduction zone. *Earth and Planetary Science Letters*, *317*–*318*, 343–353. <https://doi.org/10.1016/j.epsl.2011.10.042>
- Kano, M., & Kato, A. (2020). Detailed spatial slip distribution for short-term slow slip events along the Nankai subduction zone, Southwest Japan. *Journal of Geophysical Research: Solid Earth*, *125*(7), e2020JB019613. <https://doi.org/10.1029/2020JB019613>
- Kato, A., Obara, K., Igarashi, T., Tsuruoka, H., Nakagawa, S., & Hirata, N. (2012). Propagation of slow slip leading up to the 2011 Mw 9.0 Tohoku-Oki earthquake. *Science*, *335*, 705–708. <https://doi.org/10.1126/science.1215141>
- Katz, A. J., & Thompson, A. H. (1986). Quantitative prediction of permeability in porous rock. *Physical Review, B*, *34*, 8179–8181. <https://doi.org/10.1103/PhysRevB.34.8179>
- Katz, A. J., & Thompson, A. H. (1987). Prediction of rock electrical conductivity from mercury injection measurements. *Journal of Geophysical Research*, *92*, 599–607. <https://doi.org/10.1029/JB092iB01p00599>
- Kim, M. J., Schwartz, S. Y., & Bannister, S. (2011). Non-volcanic tremor associated with the March 2010 Gisborne slow slip event at the Hikurangi subduction margin, New Zealand. *Geophysical Research Letters*, *38*. <https://doi.org/10.1029/2011GL048400>
- Kodaira, S., Iidaka, T., Kato, A., Park, J.-O., Iwasaki, T., & Kaneda, Y. (2004). High pore fluid pressure may cause silent slip in the Nankai Trough. *Science*, *304*, 1295–1298. <https://doi.org/10.1126/science.1096535>
- Kominz, M. A., Patterson, K., & Odette, D. (2011). Lithology dependence of porosity in slope and deep marine sediments. *Journal of Sedimentary Research*, *81*, 730–742. <https://doi.org/10.2110/jsr.2011.60>
- Koulali, A., McClusky, S., Wallace, L., Allgeyer, S., Tregoning, P., D'Anastasio, E., & Benavente, R. (2017). Slow slip events and the 2016 Te Araroa Mw 7.1 earthquake interaction: Northern Hikurangi subduction, New Zealand. *Geophysical Research Letters*, *44*, 8336–8344. <https://doi.org/10.1002/2017GL074776>
- Leeman, J., Saffer, D., Scuderi, M., & Marone, C. (2016). Laboratory observations of slow earthquakes and the spectrum of tectonic fault slip modes. *Nature Communications*, *7*, 11104. <https://doi.org/10.1038/ncomms11104>
- Lewis, K. B. (1994). The 1500-km-long Hikurangi Channel: Trench-axis channel that escapes its trench, crosses a plateau, and feeds a fan drift. *Geo-Marine Letters*, *14*, 19–28. <https://doi.org/10.1007/bf01204467>
- Lewis, K. B., Collot, J., & Lalle, S. E. (1998). The dammed Hikurangi Trough: A channel-fed trench blocked by subducting seamounts and their wake avalanches (New Zealand–France GeodyNZ Project). *Basin Research*, *10*, 441–468. <https://doi.org/10.1046/j.1365-2117.1998.00080.x>
- Li, Y., & Wardlaw, N. C. (1986a). The influence of wettability and critical pore throat size ratio on snap-off. *Journal of Colloid and Interface Science*, *109*(2), 461–472. [https://doi.org/10.1016/0021-9797\(86\)90324-3](https://doi.org/10.1016/0021-9797(86)90324-3)
- Li, Y., & Wardlaw, N. C. (1986b). Mechanisms of nonwetting phase trapping during imbibition at slow rates. *Journal of Colloid and Interface Science*, *109*(2), 473–486. [https://doi.org/10.1016/0021-9797\(86\)90325-5](https://doi.org/10.1016/0021-9797(86)90325-5)
- Liu, Y., & Rice, J. R. (2007). Spontaneous and triggered aseismic deformation transients in a subduction fault model. *Journal of Geophysical Research*, *112*. <https://doi.org/10.1029/2007JB004930>
- Marschall, D., Gardner, J. S., Mardon, D., & Coates, R. (1995). *Method for correlating NMR relaxometry and Mercury injection data*. SCA Conference Paper Number 9511.
- McCaffrey, R., Wallace, L. M., & Beavan, J. (2008). Slow slip and frictional transition at low temperature at the Hikurangi subduction zone. *Nature Geoscience*, *1*, 316–320. <https://doi.org/10.1038/ngeo178>
- Meiboom, S., & Gill, D. (1958). Modified spin-echo method for measuring nuclear relaxation times. *Review of Scientific Instruments*, *29*(8), 688–691. <https://doi.org/10.1063/1.1716296>
- Mondol, N. H., Bjørlykke, K., Jahren, J., & Høeg, K. (2007). Experimental mechanical compaction of clay mineral aggregates—Changes in physical properties of mudstones during burial. *Marine and Petroleum Geology*, *24*, 289–311. <https://doi.org/10.1016/j.marpetgeo.2007.03.006>
- Morgan, J., Fagereng, A., Savage, H. M., Wang, M., Meneghini, F., Barnes, P., et al. (2018). *Seafloor overthrusting creates ductilely deformed fault rocks in marine sediments at the Hikurangi margin: Implications for fault zone evolution and mechanics at IODP site U1518*. AGU Fall Meeting 2018.
- Mouslopoulou, V., Saltogianni, V., Nicol, A., Oncken, O., Begg, J., Babeyko, A., et al. (2019). Breaking a subduction-termination from top to bottom: The large 2016 Kaikōura earthquake, New Zealand. *Earth and Planetary Science Letters*, *506*, 221–230. <https://doi.org/10.1016/j.epsl.2018.10.020>
- Nakajima, J., & Uchida, N. (2018). Repeated drainage from megathrusts during episodic slow slip. *Nature Geoscience*, *11*(5), 351–356. <https://doi.org/10.1038/s41561-018-0090-z>
- Nishiyama, N., & Yokoyama, T. (2014). Estimation of permeability of sedimentary rocks by applying water-expulsion porosimetry to Katz and Thompson model. *Engineering Geology*, *177*, 75–82. <https://doi.org/10.1016/j.enggeo.2014.05.016>
- Obara, K., & Kato, A. (2016). Connecting slow earthquakes to huge earthquakes. *Science*, *353*, 253–257. <https://doi.org/10.1126/science.aaf1512>

- Pastén-Araya, F., Potin, B., Ruiz, S., Zerbst, L., Aden-Antoniów, F., Azúa, K., et al. (2021). Seismicity in the upper plate of the Northern Chilean offshore forearc: Evidence of splay fault south of the Mejillones Peninsula. *Tectonophysics*, *800*, 228706. <https://doi.org/10.1016/j.tecto.2020.228706>
- Pedley, K. L., Barnes, P. M., Pettinga, J. R., & Lewis, K. B. (2010). Seafloor structural geomorphic evolution of the accretionary frontal wedge in response to seamount subduction, Poverty Indentation, New Zealand. *Marine Geology*, *270*(1–4), 119–138. <https://doi.org/10.1016/j.margeo.2009.11.006>
- Peterson, D. E., & Keranen, K. M. (2019). A high wave speed basal sedimentary layer identified from seismic imaging of the plate boundary in central Cascadia. *Journal of Geophysical Research: Solid Earth*, *124*, 6832–6847. <https://doi.org/10.1029/2018JB017227>
- Plaza-Faverola, A., Henrys, S., Pecher, I., Wallace, L., & Klaeschen, D. (2016). Splay fault branching from the Hikurangi subduction shear zone: Implications for slow slip and fluid flow. *Geochemistry, Geophysics, Geosystems*, *17*(12), 5009–5023. <https://doi.org/10.1002/2016GC006563>
- Revil, A., Cathles, L. M., III, Losh, S., & Nunn, J. A. (1998). Electrical conductivity in shaly sands with geophysical applications. *Journal of Geophysical Research*, *103*, 23925–23936. <https://doi.org/10.1029/98JB02125>
- Rosener, M., & Géraud, Y. (2007). Using physical properties to understand the porosity network geometry evolution in gradually altered granites in damage zones. *Geological Society, London, Special Publications*, *284*, 175–184. <https://doi.org/10.1144/SP284.12>
- Rubey, W. W., & Hubbert, M. K. (1959). Role of fluid pressure in mechanics of overthrust faulting. II. Overthrust belt in geosynclinal area of western Wyoming in light of fluid-pressure hypothesis. *Geological Society of America Bulletin*, *70*, 167–206. [https://doi.org/10.1130/0016-7606\(1959\)70\[167:rofpm\]2.0.co;2](https://doi.org/10.1130/0016-7606(1959)70[167:rofpm]2.0.co;2)
- Saffer, D. M. (2003). Pore pressure development and progressive dewatering in underthrust sediments at the Costa Rica subduction margin: Comparison with northern Barbados and Nankai. *Journal of Geophysical Research*, *108*(B5), 2261. <https://doi.org/10.1029/2002JB001787>
- Saffer, D. M., Silver, E. A., Fisher, A. T., Tobin, H., & Moran, K. (2000). Inferred pore pressures at the Costa Rica subduction zone: Implications for dewatering processes. *Earth and Planetary Science Letters*, *177*(3–4), 193–207. [https://doi.org/10.1016/S0012-821X\(00\)00048-0](https://doi.org/10.1016/S0012-821X(00)00048-0)
- Saffer, D. M., & Tobin, H. J. (2011). Hydrogeology and mechanics of subduction zone forearcs: Fluid flow and pore pressure. *Annual Review of Earth and Planetary Sciences*, *39*, 157–186. <https://doi.org/10.1146/annurev-earth-040610-133408>
- Saffer, D. M., & Wallace, L. M. (2015). The frictional, hydrologic, metamorphic and thermal habitat of shallow slow earthquakes. *Nature Geoscience*, *8*, 594–600. <https://doi.org/10.1038/ngeo2490>
- Saffer, D. M., Wallace, L. M., Barnes, P. M., Pecher, I. A., Petronotis, K. E., LeVay, L. J., et al. (2019a). Expedition 372B/375 summary. In L. M. Wallace, D. M. Saffer, P. M. Barnes, I. A. Pecher, K. E. Petronotis, & L. J. LeVay (Eds.), *Hikurangi subduction margin coring, logging, and observatories* (Vol. 372B/375). Proceedings of the International Ocean Discovery Program. <https://doi.org/10.14379/iodp.proc.372B375.101.2019>
- Saffer, D. M., Wallace, L. M., Barnes, P. M., Pecher, I. A., Petronotis, K. E., LeVay, L. J., et al. (2019b). Site U1518. In L. M. Wallace, D. M. Saffer, P. M. Barnes, I. A. Pecher, K. E. Petronotis, & L. J. LeVay (Eds.), *Hikurangi subduction margin coring, logging, and observatories* (Vol. 372B/375). Proceedings of the International Ocean Discovery Program. <https://doi.org/10.14379/iodp.proc.372B375.103.2019>
- Saito, S., & Goldberg, D. (1997). Evolution of tectonic compaction in the Barbados accretionary prism: Estimates from logging-while-drilling. *Earth and Planetary Science Letters*, *148*, 423–432. [https://doi.org/10.1016/S0012-821X\(97\)00056-3](https://doi.org/10.1016/S0012-821X(97)00056-3)
- Salles, F., Beurroies, I., Bildstein, O., Jullien, M., Raynal, J., Denoyel, R., & Damme, H. V. (2008). A calorimetric study of mesoscopic swelling and hydration sequence in solid Na-montmorillonite. *Applied Clay Science*, *39*, 186–201. <https://doi.org/10.1016/j.clay.2007.06.001>
- Schwartz, S. Y., & Rokosky, J. M. (2007). Slow slip events and seismic tremor at circum-Pacific subduction zones: Slow slip and seismic tremor. *Reviews of Geophysics*, *45*. <https://doi.org/10.1029/2006RG000208>
- Screaton, E., Saffer, D., Henry, P., & Hunze, S. (2002). Porosity loss within the underthrust sediments of the Nankai accretionary complex: Implications for overpressures. *Geology*, *30*, 19. [https://doi.org/10.1130/0091-7613\(2002\)030<0019:plwtus>2.0.co;2](https://doi.org/10.1130/0091-7613(2002)030<0019:plwtus>2.0.co;2)
- Seno, T. (2002). Tsunami earthquakes as transient phenomena. *Geophysical Research Letters*, *29*, 58–1–58–4. <https://doi.org/10.1029/2002GL014868>
- Shaddox, H. R., & Schwartz, S. Y. (2019). Subducted seamount diverts shallow slow slip to the forearc of the northern Hikurangi subduction zone, New Zealand. *Geology*, *47*, 415–418. <https://doi.org/10.1130/G45810.1>
- Shelly, D. R., Beroza, G. C., Iden, S., & Nakamura, S. (2006). Low frequency earthquakes in Shikoku, Japan, and their relationship to episodic tremor and slip. *Nature*, *442*, 188–191. <https://doi.org/10.1038/nature04931>
- Sibson, R. H. (1990). Conditions for fault-valve behaviour. *Geological Society, London, Special Publications*, *54*(1), 15–28. <https://doi.org/10.1144/GSL.SP.1990.054.01.02>
- Sing, K. S., Everett, D. H., Haul, R. A. W., Moscou, L., Pierotti, R. A., Rouquerol, J., & Siemieniowsha, T. (1985). Reporting physisorption data for gas/solid systems with special reference to the determination of surface area and porosity. *Pure and Applied Chemistry*, *54*(11), 2201–2218. <https://doi.org/10.1351/pac198254112201>
- Smith, J. E. (1971). The dynamics of shale compaction and evolution of pore-fluid pressures. *Journal of the International Association for Mathematical Geology*, *3*, 239–263. <https://doi.org/10.1007/BF02045794>
- Song, T. A., Helmberger, D. V., Brudzinski, M. R., Clayton, R. W., Davis, P., Perez-Campos, X., & Singh, S. K. (2009). Subducting slab ultra-slow velocity layer coincident with silent earthquakes in southern Mexico. *Science*, *324*, 502–506. <https://doi.org/10.1126/science.1167595>
- Tessier, A., Campbell, P. G. C., & Bisson, M. (1979). Sequential extraction procedure for the speciation of particulate trace metals. *Analytical Chemistry*, *51*(7), 844–851. <https://doi.org/10.1021/ac50043a017>
- Tobin, H., Vannucchi, P., & Meschede, M. (2001). Structure, inferred mechanical properties, and implications for fluid transport in the décollement zone, Costa Rica convergent margin. *Geology*, *29*(10), 907–910. [https://doi.org/10.1130/0091-7613\(2001\)029<0907:simpai>2.0.co;2](https://doi.org/10.1130/0091-7613(2001)029<0907:simpai>2.0.co;2)
- Todd, E. K., & Schwartz, S. Y. (2016). Tectonic tremor along the northern Hikurangi Margin, New Zealand, between 2010 and 2015. *Journal of Geophysical Research: Solid Earth*, *121*(12), 8706–8719. <https://doi.org/10.1002/2016JB013480>
- Todd, E. K., Schwartz, S. Y., Mochizuki, K., Wallace, L. M., Sheehan, A. F., Webb, S. C., et al. (2018). Earthquakes and tremor linked to seamount subduction during shallow slow slip at the Hikurangi margin, New Zealand. *Journal of Geophysical Research: Solid Earth*, *123*(8), 6769–6783. <https://doi.org/10.1029/2018JB016136>
- Tudge, J., & Tobin, H. J. (2013). Velocity-porosity relationships in smectite-rich sediments: Shikoku Basin, Japan. *Geochemistry, Geophysics, Geosystems*, *14*(12), 5194–5207. <https://doi.org/10.1002/2013GC004974>
- Uchida, N., Inuma, T., Nadeau, R. M., Burgmann, R., & Hino, R. (2016). Periodic slow slip triggers megathrust zone earthquakes in north-eastern Japan. *Science*, *351*, 488–492. <https://doi.org/10.1126/science.1231088>

- Uchida, N., Takagi, R., Asano, Y., & Obara, K. (2020). Migration of shallow and deep slow earthquakes toward the locked segment of the Nankai megathrust. *Earth and Planetary Science Letters*, 531, 115986. <https://doi.org/10.1016/j.epsl.2019.115986>
- Underwood, M. B., Dans Wallace, L. M., Saffer, D. M., Barnes, P. M., Pecher, I. A., Petronotis, K. E., et al. (2021). Data report: Clay mineral assemblages within trench-floor and accreted trench-floor deposits, IODP Expedition 372B/375 Sites U1518 and U1520, offshore New Zealand. In Hikurangi subduction margin coring, logging, and observatories (Vol. 372B/375). Proceedings of the International Ocean Discovery Program. <https://doi.org/10.14379/iodp.proc.372B375.206.2021>
- Vallée, M., Nocquet, J.-M., Battaglia, J., Font, Y., Segovia, M., Régnier, M., et al. (2013). Intense interface seismicity triggered by a shallow slow slip event in the Central Ecuador subduction zone. *Journal of Geophysical Research: Solid Earth*, 118(6), 2965–2981. <https://doi.org/10.1002/jgrb.50216>
- Wallace, L. M. (2020). Slow slip events in New Zealand. *Annual Review of Earth and Planetary Sciences*, 48, 175–203. <https://doi.org/10.1146/annurev-earth-071719-055104>
- Wallace, L. M., & Beavan, J. (2006). A large slow slip event on the central Hikurangi subduction interface beneath the Manawatu region, North Island, New Zealand. *Geophysical Research Letters*, 33, 11. <https://doi.org/10.1029/2006GL026009>
- Wallace, L. M., & Beavan, J. (2010). Diverse slow slip behavior at the Hikurangi subduction margin, New Zealand. *Journal of Geophysical Research*, 115, B12402. <https://doi.org/10.1029/2010JB007717>
- Wallace, L. M., Beavan, J., Bannister, S., & Williams, C. (2012). Simultaneous long-term and short-term slow slip events at the Hikurangi subduction margin, New Zealand: Implications for processes that control slow slip event occurrence, duration, and migration. *Journal of Geophysical Research*, 117, B11402. <https://doi.org/10.1029/2012JB009489>
- Wallace, L. M., Beavan, J., McCaffrey, R., & Desmond, D. (2004). Subduction zone coupling and tectonic block rotations in the North Island, New Zealand. *Journal of Geophysical Research*, 109, B12406. <https://doi.org/10.1029/2004JB003241>
- Wallace, L. M., Kaneko, Y., Hreinsdóttir, S., Hamling, I., Peng, Z., Bartlow, N., et al. (2017). Large-scale dynamic triggering of shallow slow slip enhanced by overlying sedimentary wedge. *Nature Geoscience*, 10, 765–770. <https://doi.org/10.1038/ngeo3021>
- Wallace, L. M., Reyners, M., Cochran, U., Bannister, S., Barnes, P. M., Berryman, K., et al. (2009). Characterizing the seismogenic zone of a major plate boundary subduction thrust: Hikurangi Margin, New Zealand. *Geochemistry, Geophysics, Geosystems*, 10(10), 1–32. <https://doi.org/10.1029/2009GC002610>
- Wallace, L. M., Saffer, D. M., Barnes, P. M., Pecher, I. A., Petronotis, K. E., LeVay, L. J., et al. (2019). Expedition 372B/375 methods. In L. M. Wallace, D. M. Saffer, P. M. Barnes, I. A. Pecher, K. E. Petronotis, & L. J. LeVay (Eds.), *Hikurangi subduction margin coring, logging, and observatories* (Vol. 372B/375). Proceedings of the International Ocean Discovery Program. <https://doi.org/10.14379/iodp.proc.372B375.102.2019>
- Wallace, L. M., Webb, S. C., Ito, Y., Mochizuki, K., Hino, R., Henrys, S., et al. (2016). Slow slip near the trench at the Hikurangi subduction zone, New Zealand. *Science*, 352, 701–704. <https://doi.org/10.1126/science.aaf2349>
- Warren-Smith, E., Fry, B., Wallace, L., Chon, E., Henrys, S., Sheehan, A., et al. (2019). Episodic stress and fluid pressure cycling in subducting oceanic crust during slow slip. *Nature Geoscience*, 12, 475–481. <https://doi.org/10.1038/s41561-019-0367-x>
- Webb, T. H., & Anderson, H. (1998). Focal mechanisms of large earthquakes in the North Island of New Zealand: Slip partitioning at an oblique active margin. *Geophysical Journal International*, 134(1), 40–86. <https://doi.org/10.1046/j.1365-246x.1998.00531.x>
- Wendt, J., Oglesby, D. D., & Geist, E. L. (2009). Tsunamis and splay fault dynamics. *Geophysical Research Letters*, 36, 15. <https://doi.org/10.1029/2009GL038295>
- Williams, C. A., Eberhart-Phillips, D., Bannister, S., Barker, D. H. N., Henrys, S., Reyners, M., & Sutherland, R. (2013). Revised interface geometry for the Hikurangi subduction zone, New Zealand. *Seismological Research Letters*, 84, 1066–1073. <https://doi.org/10.1785/0220130035>
- Yamashita, Y., Yakiwara, H., Asano, Y., Shimizu, H., Uchida, K., Hirano, S., et al. (2015). Migrating tremor off southern Kyushu as evidence for slow slip of a shallow subduction interface. *Science*, 348, 676–679. <https://doi.org/10.1126/science.aaa4242>
- Yokota, Y., & Ishikawa, T. (2020). Shallow slow slip events along the Nankai Trough detected by GNSS-A. *Science Advances*, 6, 3. <https://doi.org/10.1126/sciadv.aay5786>